Volume 61
Number 8
25 January 2025
Pages 1473–1706

ChemComm

Chemical Communications

rsc.li/chemcomm

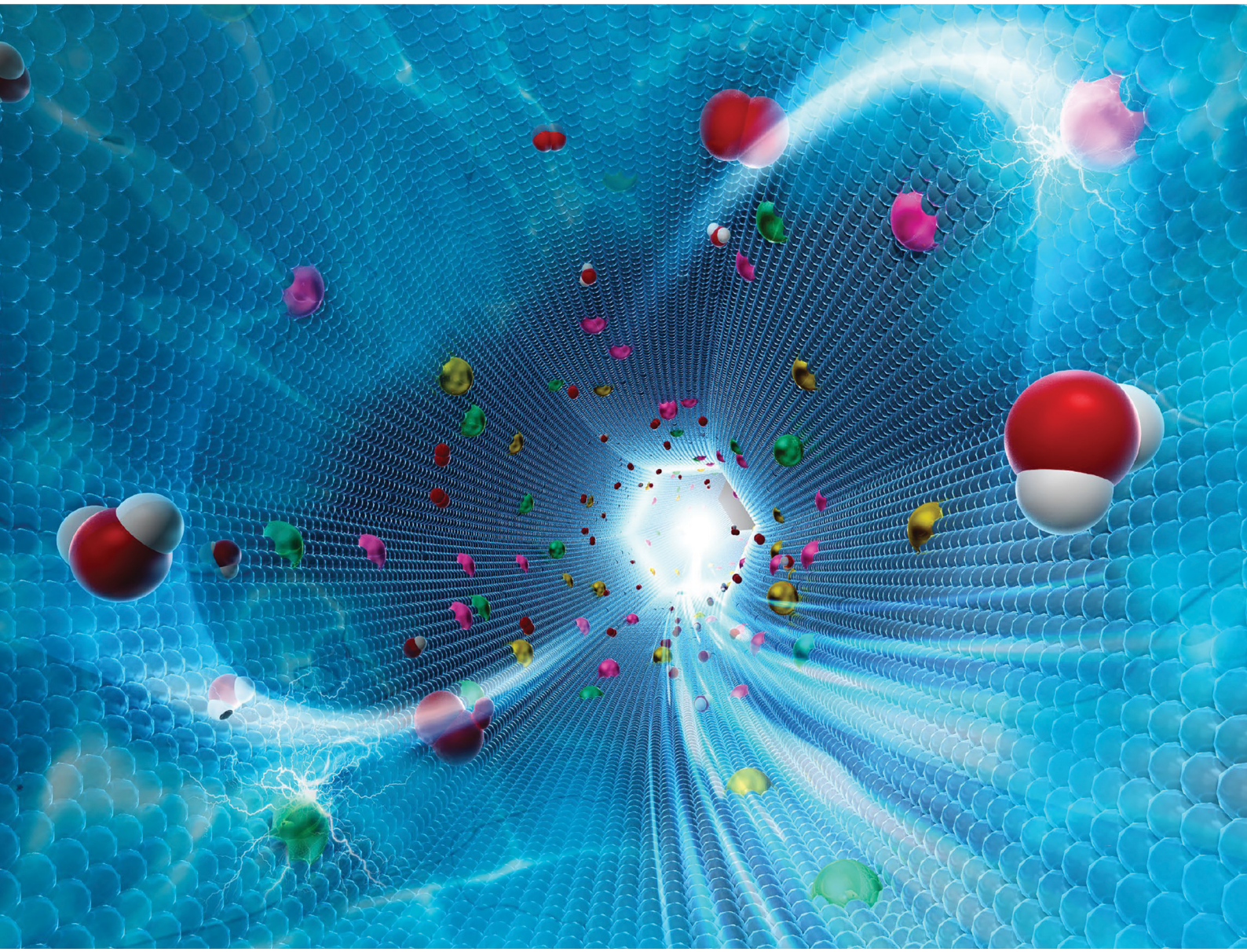

ISSN 1359-7345

ROYAL SOCIETY OF CHEMISTRY

FEATURE ARTICLE

Kouki Oka, Tatsuo Kimura *et al.*

Developing porous electrocatalysts to minimize overpotential for the oxygen evolution reaction

ChemComm

FEATURE ARTICLE

View Article Online
View Journal | View Issue

Cite this: *Chem. Commun.*, 2025, **61**, 1533

Developing porous electrocatalysts to minimize overpotential for the oxygen evolution reaction

Takahiro Ami,[a] Kouki Oka, *[abc] Hitoshi Kasai[a] and Tatsuo Kimura *[d]

Received 10th October 2024,
Accepted 3rd December 2024

DOI: 10.1039/d4cc05348f

rsc.li/chemcomm

The development of electrocatalysts for the oxygen evolution reaction (**OER**) is one of the most critical issues for improving the efficiency of electrochemical water-splitting, which can produce green hydrogen energy without CO_2 emissions. This review outlines the advances in the precise design of inorganic- and organic-based porous electrocatalysts, which are designed by various strategies, to catalyze the **OER** in the electrolytic cycle for efficient water-splitting. For developing high-performance electrocatalysts with low overpotentials, it is important to design a chemical composition that optimizes binding energy for an intermediate in the **OER** and allows the easy access of reactants to active sites depending on the porosity of electrocatalysts. Porous structures give us the positive opportunity to increase the accessible surface of active sites and effective diffusion of targeting molecules, which is potentially one of the guidelines for developing active electrocatalysts. Further modification of the frameworks is also powerful for tailoring the function of pore surfaces and the environment of inner spaces. Designable organic molecules can also be embedded inside inorganic- and organic-based frameworks. According to chemical composition (inorganic and organic), nanostructure (crystalline and amorphous) and additional modification (metal doping and organic design) of porous electrocatalysts, the current status of resultant **OER** performance is surveyed with some problems that should be solved for improving the **OER** activity. The remarkable progress in **OER** electrocatalysts is also introduced for demonstrating the bifunctional hydrogen evolution reaction (**HER**) and for utilizing seawater.

1. Introduction

To deal with global warming, which has advanced increasingly in recent years, all countries around the world must make significant efforts to realize a carbon-neutral society. Electrochemical water-splitting has attracted much attention as a clean energy production technology, which can produce hydrogen (H_2) with minimum carbon dioxide (CO_2) emission by utilizing renewable energy (*e.g.*, sunlight energy and wind energy).[1] Hydrogen is expected to be a next-generation carbon-free energy source, having the highest gravimetric energy density.[2] The electrochemical water-splitting mainly proceeds through the oxygen evolution reaction (**OER**) at the anode and the hydrogen evolution reaction (**HER**) at the cathode. However, the **OER** is a bottleneck in electrochemical water-splitting because the overpotential of the **OER** is one order of magnitude greater than that of the **HER**.[3–6] The benchmarks for practical **OER** electrocatalysts are iridium oxide (IrO_2) and ruthenium oxide (RuO_2), showing a current density of 10 mA cm^{-2} at overpotentials of around 300–400 mV, although these precious metal-based catalysts need substantial resource costs.[7] In fact, more than 90 tons of Ir is needed to supplement hydrogen production from hydrocarbons (annual production of more than 70 million tons) by the current water-splitting technology. Considering that the global reserves and annual production of Ir are approximately 1000[8] and 8 tons,[9] respectively, this task is unrealistic.

Earth-abundant base metals, such as iron (Fe), cobalt (Co) and nickel (Ni), that are produced more than 1000 times than that of Ir and Ru per year,[10,11] exhibit excellent **OER** activity. Such base metal derivative materials have been investigated aggressively for the development of inexpensive **OER** electrocatalysts with low overpotentials.[12–14] In addition, electrochemical water-splitting involves high costs owing to the need for expensive equipment and large amount of freshwater to provide enough hydrogen. Hence, in recent years, bifunctional **OER-HER** and innovative **OER** electrocatalysts are strongly recommended to reduce equipment costs and/or to explore the possibility of utilizing unlimited seawater. Many studies have focused on the nanostructural design of base metal

[a] *Institute of Multidisciplinary Research for Advanced Materials, Tohoku University, 2-1-1 Katahira, Aoba-ku, Sendai, Miyagi 980-8577, Japan*
[b] *Carbon Recycling Energy Research Center, Ibaraki University, 4-12-1 Nakanarusawa, Hitachi, Ibaraki 316-8511, Japan*
[c] *Deuterium Science Research Unit, Center for the Promotion of Interdisciplinary Education and Research, Kyoto University, Yoshida, Sakyo-ku, Kyoto 606-8501, Japan*
[d] *National Institute of Advanced Industrial Science and Technology (AIST), Sakurazaka, Moriyama-ku, Nagoya 463-8560, Japan. E-mail: t-kimura@aist.go.jp*

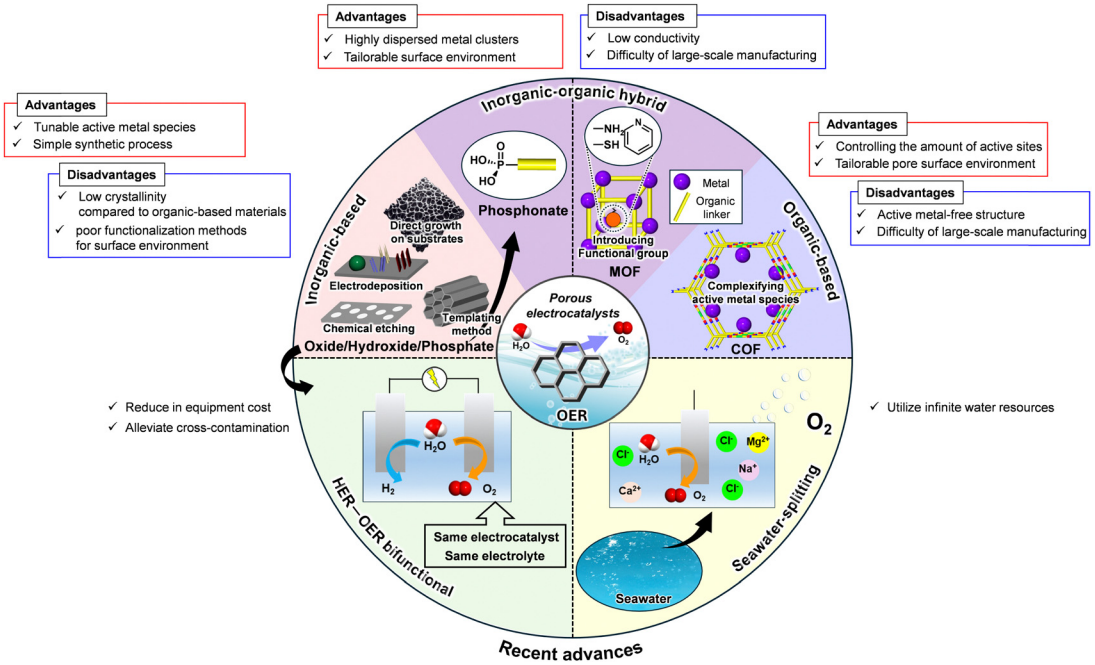

Fig. 1 Summary of the characteristics and recent advances in porous **OER** electrocatalysts.

derivative electrocatalysts to maximize **OER** activity.[15–17] (See Fig. 1) Highly porous structures are one of the most attractive structural features, having a great potential to enhance **OER** activity depending on many active sites and high diffusivity arising from high specific surface area, large pore volume and tunable pore shape/size.[18–20] Further design of porous surfaces is possible for tailoring not only major physical properties but also functions of pore surfaces[21,22] and the environment inside pores[23,24] by modification with constituent molecules, feasibly enhancing uptake potential and unique interaction at the resultant pore surfaces against specific substances.

In our recent work, organic-based porous materials have been designed by controlling organic components, and surface environments are assessed by the introduction of substituents into constituent molecules.[25–29] Basic and highly hydrophobic pore surfaces are designed with the fabrication of all-organic porous materials, enabling selective CO_2 adsorption[30] and improving the proton conductivity.[31] Even in the application of **OER** electrocatalysts, porous materials can adjust properties (*e.g.*, wettability, electron conductivity, and proton conductivity) against the reactants and products. Organic-based porous materials enable the precise control of their structures to confirm the effect of specific properties on **OER** activity and then help elucidate the **OER** mechanism on the microscopic scale. Inorganic-based porous materials can tune the composition of active metal species and then help elucidate the **OER** mechanism on the macroscopic scale. From this viewpoint, it is crucial to summarize the effects of compositions, nanostructures and properties on **OER** activities based on inorganic- and organic-based porous materials to systematically understand the **OER** mechanism as well as the material design of **OER** electrocatalysts.

Many reviews have been reported to date in the field of **OER** electrocatalysts and most of them focus on the material composition. This feature article focuses on a variety of porous electrocatalysts to maximize the **OER** performance in addition to the compositional design of the latest **OER** electrocatalysts for revealing the effects of the chemical composition of electrocatalysts, the design of porous structures and the additional modification of organic molecule. Besides, we survey the significant advances in **OER-HER** bifunctional electrocatalysts to catalyze not only **OER** at the anode but also **HER** at the cathode as well as those **OER** electrocatalysts that enable the use of seawater and thus provide the guidelines to design high-performance porous electrodes for the development of **OER** electrocatalysts (see Fig. 1).

2. Overview of electrodes for electrochemical water-splitting

The overall electrochemical water-splitting reaction is expressed by reaction (1) in Fig. 2. By applying a voltage and passing an electric current through the electrolyzer (see Fig. 2), electrons move between the cathode and the anode for the **OER** and **HER** reactions. The electrolyte membrane allows the transfer of only specific ions necessary for the electrode reaction without transferring electrons. The electrocatalysts on each electrode contribute to the reduction of activation energy in the electrochemical reaction and suppress the energy loss in the electrolyzer. Currently, Ru/IrO_2 and Pt have been used as electrocatalysts general for the cathode and the anode, respectively.

The Gibbs free energy change (ΔG°) for the electrochemical water-splitting is +237.2 kJ mol^{-1} under the standard conditions (activities of all species; 1, ambient pressure; 1 atm,

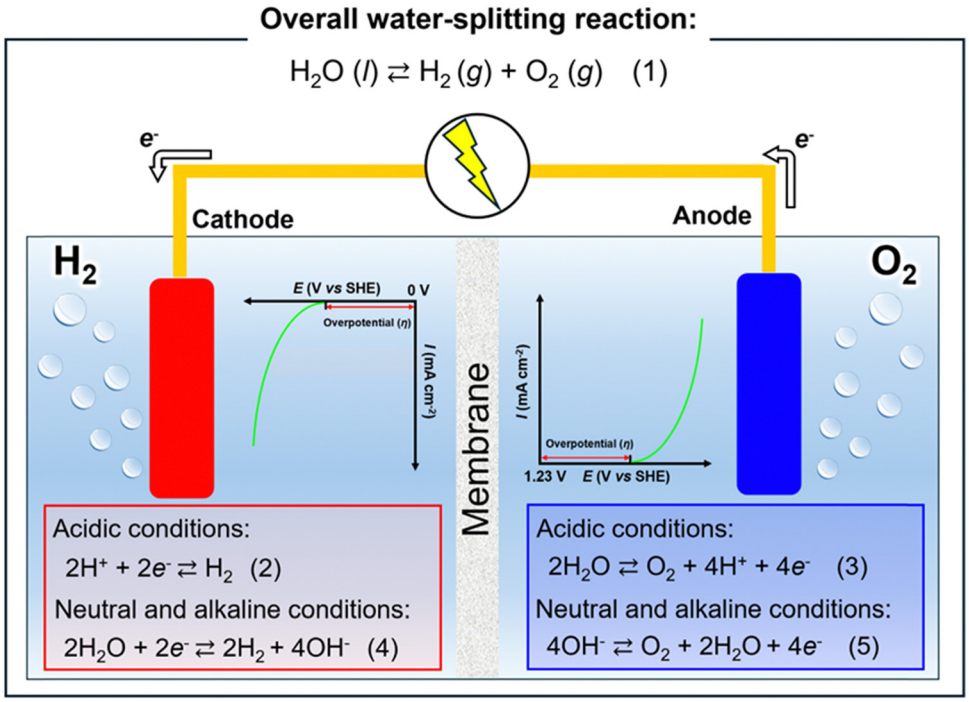

Fig. 2 Overview of the overall water-splitting reaction.

temperature; 298.15 K).[32] ΔG° can be converted to the standard potential (E°, theoretical cell voltage of the electrolytic reaction) for the entire equilibrium reaction by eqn (1):

$$\Delta G^\circ = -nFE^\circ \quad (1)$$

n and F are the number of electrons and Faraday's constant (9.649×10^4 C mol^{-1}), respectively. In the calculation from eqn (1), the electrochemical water-splitting reaction requires the thermodynamic voltage of 1.23 V to proceed in the cell.

The electrochemical water-splitting reaction consists of **HER** at the cathode and **OER** at the anode, as described by reactions (2) and (3) in Fig. 2 under acidic conditions.[33,34] Reaction (2) represents the electrode reaction at a standard hydrogen electrode (**SHE**) where E° is 0.00 V (*vs.* **SHE**). ΔG° of reaction (3) is -237.2 kJ mol^{-1},[32] and E° is calculated to be +1.23 V (*vs.* **SHE**) by eqn (1).

HER produces hydrogen by the reduction of water, like reaction (4) in Fig. 2, not protons, under neutral and alkaline conditions.[33,34] ΔG° of reaction (4) is +159.8 kJ mol^{-1},[32] and E° is calculated to be -0.828 V (*vs.* **SHE**) by eqn (1). The **OER** corresponding to reaction (4) (reaction (5) in Fig. 2) is represented by the oxidation of water (reaction (3)) and the oxidation of the hydroxide anion produced by reaction (4). E° of reaction (5) is calculated to be +0.401 V (*vs.* **SHE**) based on the ΔG° of reaction (3) (-237.2 kJ mol^{-1}). The reduction reaction (Ox + ne$^-$ ⇄ Red), in which the oxidized species (Ox) forms the reduced species (Red), is in electrochemical equilibrium and follows eqn (2) (Nernst's equation).

$$E = E^\circ + \frac{nF}{RT} \ln \frac{a_{ox}}{a_{red}} \quad (2)$$

E is the equilibrium potential, and R, T, and a_i are the universal gas constant, the temperature, and the activity of species i. By applying eqn (2) to **HER** (reactions (2) and (4)), following eqn (3) is obtained in both cases.[35]

$$E = (-0.059 \times \text{pH})\ \text{V}\ (\textit{vs.}\ \textbf{SHE}) \quad (3)$$

Furthermore, by applying eqn (2) to **OER** (reactions (3) and (5)), eqn (4) is obtained in both cases.[35]

$$E = (+1.23 - 0.059 \times \text{pH})\ \text{V}\ (\textit{vs.}\ \textbf{SHE}) \quad (4)$$

Therefore, the theoretical (minimum) cell voltage for electrochemical water-splitting is 1.23 V under all pH conditions.

Practical water electrolyzers require a working voltage higher than the theoretical cell voltage for electrochemical water-splitting (1.23 V), which is attributed to the overpotentials on both **HER** and **OER** electrodes.[36] In particular, the **OER**, through a complex four-electron reaction with multiple intermediates, proceeds with a much larger overpotential than the two-electron **HER**.[3–7,37,38] To accelerate the overall electrochemical water-splitting reaction, highly active **OER** electrocatalysts should be required to minimize the overpotential. The theoretical overpotential of **OER** is confirmed by following the oxygen adsorption energy of the catalyst surface.[36] A strong interaction between the reaction intermediates and the catalyst surface needs excess energy to desorb oxygen (O_2) molecules. If such an interaction is too weak, the **OER** does not proceed efficiently. To minimize the overpotential for **OER**, appropriate control of the oxygen adsorption energy on the catalyst surface is quite important.[39]

It is rational to consider that **OER** proceeds through two possible reaction mechanisms (see Fig. 3) called the adsorbate evolution mechanism and lattice-oxygen oxidation mechanism.[14] Both mechanisms involve four proton–electron transfer reactions

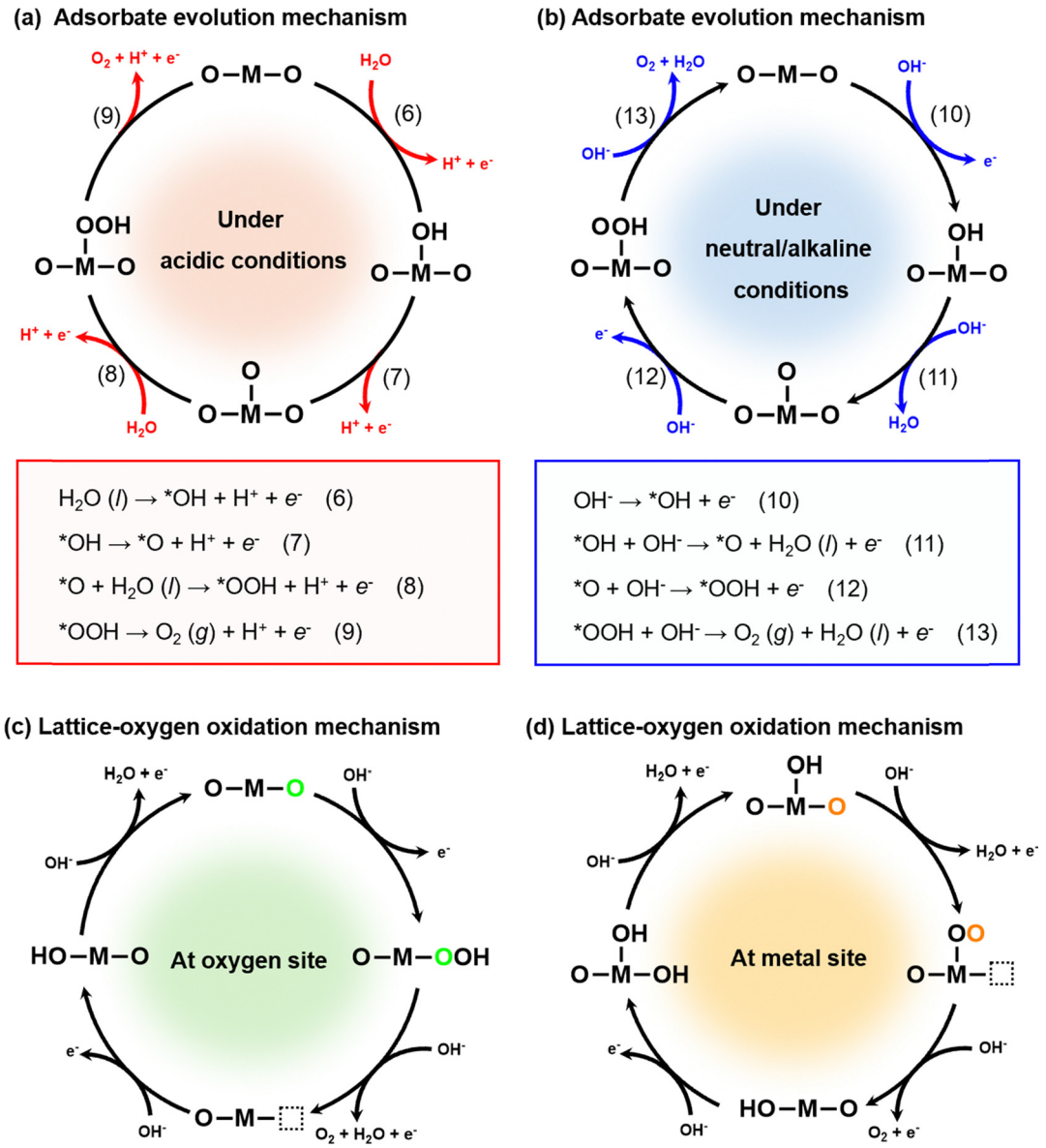

Fig. 3 Proposed adsorbate evolution mechanisms for the **OER** (a) under acidic conditions and (b) under neutral and alkaline conditions. Proposed lattice-oxygen oxidation mechanism for the **OER** (c) at the oxygen site and (d) at the metal site. *O indicates an oxygen atom adsorbed on the active metal species.

and lead to the production of gaseous O_2 from water (H_2O) on the active site and through lattice oxygen, respectively. Especially, the adsorbate evolution mechanism is completed with four steps, such as reactions (6)–(9) under acidic conditions (Fig. 3a) and reactions (10)–(13) under neutral/alkaline conditions (Fig. 3b). In this mechanism, **OER** activity is limited by the scaling relationship of the adsorption energy between *OH/*OOH intermediates.[40] The theoretical minimum overpotential is considered to be 370 mV for the adsorbate evolution mechanism.[41] Besides, two mechanisms *via* different active centers have been proposed for the lattice-oxygen oxidation mechanism.[42] The lattice oxygen is the active center in this mechanism (Fig. 3c). The lattice oxygen accepts the OH^- directly through a nucleophilic attack to form the *OOH intermediates. Then, the release of O_2 creates oxygen vacancy sites (□), which then adsorb OH^- to form *OH intermediates. The metal site acts as an active center to adsorb OH^- and causes a deprotonation reaction (Fig. 3d). Surface reconstruction leads to the formation of *OOH intermediates through the combination of *O species and activated lattice oxygen, releasing O_2. In both mechanisms, the lattice-oxygen oxidation mechanism can effectively avoid the adsorption of *OH/*OOH, and thus this mechanism possibly proceeds with smaller overpotentials than the theoretical minimum overpotential of 370 mV for the adsorbate evolution mechanism.[43] The **OER** mechanism mainly depends on the composition, structure, and crystallinity of electrocatalysts, but the reaction conditions predominant by the lattice-oxygen oxidation mechanism rather than the adsorbate evolution mechanism are still open for discussion.

To reduce the activation energy barrier during the **OER** cycle, the surface property of electrocatalysts, depending on the

composition and structure, has been designed using unique methods. Dai *et al.* succeeded in fabricating an electrochemically active Co_3O_4 nanosheet with a high specific surface area by a plasma-engraving strategy.[44] The nanosheet showed 10 times higher **OER** activity than conventional Co_3O_4 materials. Cao *et al.* reported that a hierarchically porous Co(OH)F material was very useful for the efficient diffusion of reactants and catalyzed **OER** with a very small overpotential of 313 mV.[45] The **OER** activity should still be improved by designing the number of active sites at the surfaces of electrocatalysts as well as the enhancement of diffusion in the nanopores of electrocatalysts. Accordingly, the precise design of nanoporous structures is one of the recent research trends in optimizing **OER** electrocatalysts.

3. Significant factors for enhancing OER activity

The overpotential (η) is defined as the difference between the actual potential at which the reaction proceeds and the theoretical equilibrium potential. It is actually difficult to measure accurate values of the overpotential and the overpotential is then determined generally by using the potential value at the constant current density in terms of the overpotential (η_{10}) at a current density of 10 mA cm^{-2}. In the case of **OER**, the overpotential is calculated as the difference between the potential at the current density (i) reaching 10 mA cm^{-2} and the equilibrium potential (1.23 V). Electrocatalysts with an overpotential in the range of 300–400 mV, comparable to the benchmark catalysts such as IrO_2 and RuO_2, have superior **OER** activity.

Tafel slope (b) is used to evaluate the reaction kinetics as well as reaction mechanisms. The Butler–Volmer equation is defined by eqn (5) as the most fundamental relationship in electrochemical kinetics.

$$i = i_0\left\{\exp\left(\frac{\alpha_a nFE}{RT}\right) + \exp\left(\frac{\alpha_c nFE}{RT}\right)\right\} \quad (5)$$

i, i_0, α_a, and α_c are current density, exchange current density, and anodic charge transfer coefficient and cathodic one, respectively. If the overpotential at the anodic electrode is high and most of the whole current is arising from the electrode, eqn (5) is simplified as the Tafel equation like eqn (6) with eqn (7) and (8).[46] The Tafel slope (b) defines how fast the current increases for an applied potential and helps determine the rate-determining step (**RDS**) and reaction mechanisms. In the single-electron reaction mechanism, the transfer coefficient (α) is treated as a symmetry factor (β) and is given by eqn (9).

$$i \approx i_0 \exp\left(\frac{\alpha_a nFE}{RT}\right) \quad (6)$$

$$\log(i) \approx \log(i_0) + \frac{\eta}{b} \quad (7)$$

$$b = \frac{\sigma\eta}{\sigma\log(i)} = \frac{2.303RT}{\alpha F} \quad (8)$$

$$\alpha = \beta = \frac{1}{2} + \frac{\eta}{\lambda} \quad (9)$$

Here, λ is reorganization energy. If the Tafel slope of the electrocatalyst is 120 mV dec^{-1}, **RDS** follows a single-electron reaction. According to Bockris and Reddy, the transfer coefficients in multi-electron reactions are formulated as,

$$\alpha_a = \frac{\eta_b}{\nu} + \eta_\gamma\beta \quad (10)$$

where η_b, ν, and η_γ are the number of electrons returned to the electrode before **RDS**, the number of **RDS** in the whole reaction, and the number of electrons involved in **RDS**, respectively. The Tafel slope and the transfer coefficient are related to the number of electrons during the reaction. The difference in the Tafel slopes shows different **RDS** and reaction mechanisms. Accordingly, **OER** electrocatalysts with a small Tafel slope show high catalytic activity. Ideally, **OER** electrocatalysts should be designed with materials that have a minimum overpotential and Tafel slope.

4. Development of porous OER electrocatalysts

The structural features of highly porous electrocatalysts give us the opportunity to enhance the catalytic performance due to the increase in the number of reaction sites and the diffusion efficiency of reactants.[18–20] Base metal-based inorganic materials, being abundant and inexpensive rather than precious metal-based ones, have been investigated as alternative electrocatalyst materials to IrO_2 and RuO_2. A wide variety of inorganic solids, such as oxides, hydroxides, and phosphates of base metals, can be designed as periodic nanoporous materials using hard and soft templating approaches.[47,48] Base metal-based porous **OER** electrocatalysts have also been synthesized so far by chemical etching,[49] in which chemical reagents react with the material to form designed nanopores; electrochemical deposition,[50] in which active species are directly loaded on the electrode surface by anodic/cathodic electrolysis of catalyst and precursor solutions; and direct growth on substrates with porous structures such as metal foams.[51] The details of the synthetic methods are explained in several review articles.[20] Inorganic materials can be designed with varying compositions of active metal species and play an important role in directly investigating the effect of active metal species.

Innovative strategies have been developed in the research fields of metal–organic framework (MOF) and covalent-organic framework (COF) type porous materials with designable organic linkers.[52–54] The synthetic strategies to tune the pore shape and surface function have been triggered with an elegant proposal as the reticular chemistry by Yaghi *et al.* since 1995.[55] Further functionalizations of organic linkers have been challenged by the precise adjustment of physical properties and careful design of nanoporous structures, attracting much attention as candidates for **OER** electrocatalysts. The utilization of MOF and COF would be beneficial for structural determination

Table 1 **OER** performance of the reported porous transition metal oxide-based **OER** catalysts

OER electrocatalyst	Substrate	Electrolyte	η_{10} (mV)	Tafel slope (mV dec^{-1})	BET surface area (m^2 g^{-1})	Pore size (nm)	Pore volume (cm^3 g^{-1})	Ref.
Co_3O_4	Carbon fiber paper	1 M KOH	409	62	37.7	—	—	62
Co_3O_4	Carbon black	1 M KOH	368	59	47.3	26.2	—	63
Co_3O_4	Ni foam	1 M KOH	311(η_{20})	76	—	—	—	64
Co_3O_4 NPs	Glassy carbon	1 M KOH	392	44	23.2	3.0	0.0082	65
Co_3O_4 NWs	Glassy carbon	1 M KOH	392	53	22.1	15.0	0.077	65
Co_3O_4 NSs	Glassy carbon	1 M KOH	394	52	24.2	4.5	0.019	65
Co_3O_4 NCs	Glassy carbon	1 M KOH	405	58	15.7	3.9	0.0040	65
DL-Co_3O_4	Ni foam	1 M KOH	256(η_{50})	61	57.4	12.6	—	66
Cl–Co_3O_4-h	Ni foam	3 M KOH	257	70	202	3.3	0.48	67
CoO_x	Glassy carbon	1 M KOH	306	65	30.4	—	—	68
CoO_x	Carbon fiber paper	1 M KOH	300	40	—	—	—	69
NiO	Ni foam	1 M KOH	310	54	—	—	—	70
NiO/$NiFe_2O_4$	ITO	0.1 M KOH	328	42	107	3.0	—	71
$Ni_xMn_{1-x}O_y$	Glassy carbon	1 M KOH	297	91	152	7.9	—	72
$Ni_xCo_{3-x}O_4$	Ni Foam	1 M KOH	287	88	118	2.0–4.0	—	73
$Ni_xCo_{3-x}O_4$	Ti foil	1 M NaOH	—	64	112	—	—	74
Ni–FeO_x	Glassy carbon	1 M KOH	284	48	—	—	—	75
$NiCo_2O_4$	Ni Foam	1 M KOH	271	172	60.7	≈3.0	0.33	76
$MnCo_2O_4$	Ni Foam	1 M KOH	289	182	26.4	≈3.0	0.11	76
$ZnCo_2O_4$	Ni Foam	1 M KOH	340	183	34.7	≈3.0	0.17	76
$(Fe_{0.2}Co_{0.2}Ni_{0.2}Cr_{0.2}Mn_{0.2})_3O_4$	Carbon paper	1 M KOH	275	50	118	1.7–5.7	—	77
Fe–Co_3O_4	Ni foam	1 M KOH	204	38	199	0.95	—	78
Fe–Co_3O_4	Glassy carbon	0.1 M KOH	486	—	110	3.0, 11.0	0.16	79
Co_2–Ni_1–O	Ni foam	1 M KOH	310	57	181	2.5	—	80
$NiCo_2O_4$	FTO	1 M KOH	565	292	71.9	—	—	81
$NiCo_2O_4$	Carbon fiber paper	0.1 M KOH	340	63	—	—	—	82
$NiCo_2O_4$	Glassy carbon	1 M KOH	230	85	—	—	—	83
$CoFe_2O_4$	Glassy carbon	1 M KOH	342	57	163.3	—	0.79	84
$CoFe_2O_4$	Glassy carbon	0.1 M KOH	408	82	61.5	4.0	—	85
$Zn_xCo_{3-x}O_4$	Ti foil	1 M KOH	320	51	78.5	3.0, 6.0	—	86
$ZnCo_2O_4$	Glassy carbon	1 M KOH	389	60	65.9	6.3	—	87
WCoO-NP	Glassy carbon	1 M KOH	270	92	142	8.3	0.24	88
NFC@CNSs	Glassy carbon	1 M KOH	256	61	145	11.7	0.50	89

because of their highly crystalline, uniform, and designable frameworks. To maximize the **OER** activity of such porous materials showing the functions arising from organic linkers, we should understand the physical and chemical properties of the clear frameworks during the water-splitting reaction.

4.1. Inorganic-based OER electrocatalysts

4.1.1. Base metal oxides. Metal oxides are potentially poor conductors and may not be an ideal candidate for **OER** electrocatalysts,[56] but this limitation can be improved by the design of porous structures, chemical compositions, and so on. For improving **OER** activity, the base metal oxide is one of the potential candidates for an **OER** electrocatalyst showing high activity and enough stability based on the corrosion resistance during the reaction.[4,36,57] In this case, the surface oxyhydroxide layer is formed under the **OER** conditions and acts as the effective active site.[58–60] Various base metal oxide-based porous **OER** electrocatalysts, such as mono- and multi-metal (including cobalt, nickel, and iron) oxides, have been reported so far (see Table 1), and most of them have higher specific surface area than non-porous ones. In most cases, the activity of **OER** electrocatalysts is evaluated under highly alkaline conditions with pH > 13. This is because, in addition to the fact that base metal oxides are generally unstable under acidic conditions,[34] active oxyhydroxide layers are stable under alkaline conditions.[61] The overpotential is measured using conductive substrates such as graphitic carbon, transparent glass (*e.g.*, indium tin oxide and fluorine-doped tin oxide) and metal foam (*e.g.*, nickel foam) and described as η_i at the current density reaching i mA cm^{-2}; for example η_{10} is the overpotential when the current density reaches 10 mA cm^{-2}. Even in cases using the same electrocatalyst, the electrochemical property of conductive substrates also contributes to the **OER** activity. In particular, metal foams improve the total porosity of designed electrodes and/or the specific surface area of active layers, leading to an excellent overpotential.

A monometallic cobalt oxide (Co_3O_4), one of the 3d transition metal oxides, has been widely investigated as an **OER** electrocatalyst. Transition metals, such as cobalt, nickel and iron, exhibit redox activity and are suitable as catalysts for electrochemical reactions. Xie *et al.* succeeded in fabricating a porous Co_3O_4 nanosheet at the atomic scale by fast-heating strategy using an intermediate precursor of an atomically-thick CoO nanosheet (see Fig. 4a).[90] The ultrathin thickness of 0.43 nm afforded 5-coordinated Co^{3+} and 4-/3-coordinated pore-surrounding Co^{3+} atoms. The high pore occupancy facilitated easy electrolyte infiltration and ensured a large contact area with the electrolyte, thus enlarging the reaction space. This Co_3O_4 porous nanosheet yielded a highly dense current of up to 341.7 mA cm^{-2} at 1.0 V *vs.* Ag/AgCl. Paik *et al.* synthesized a porous Co_3O_4 nanosheet by a graphene-templated method (see Fig. 4b). This Co_3O_4 nanosheet showed an excellent **OER** overpotential of 368 mV at 10 mA cm^{-2}, comparable to the benchmark catalyst (RuO_2).[63] Yin *et al.*

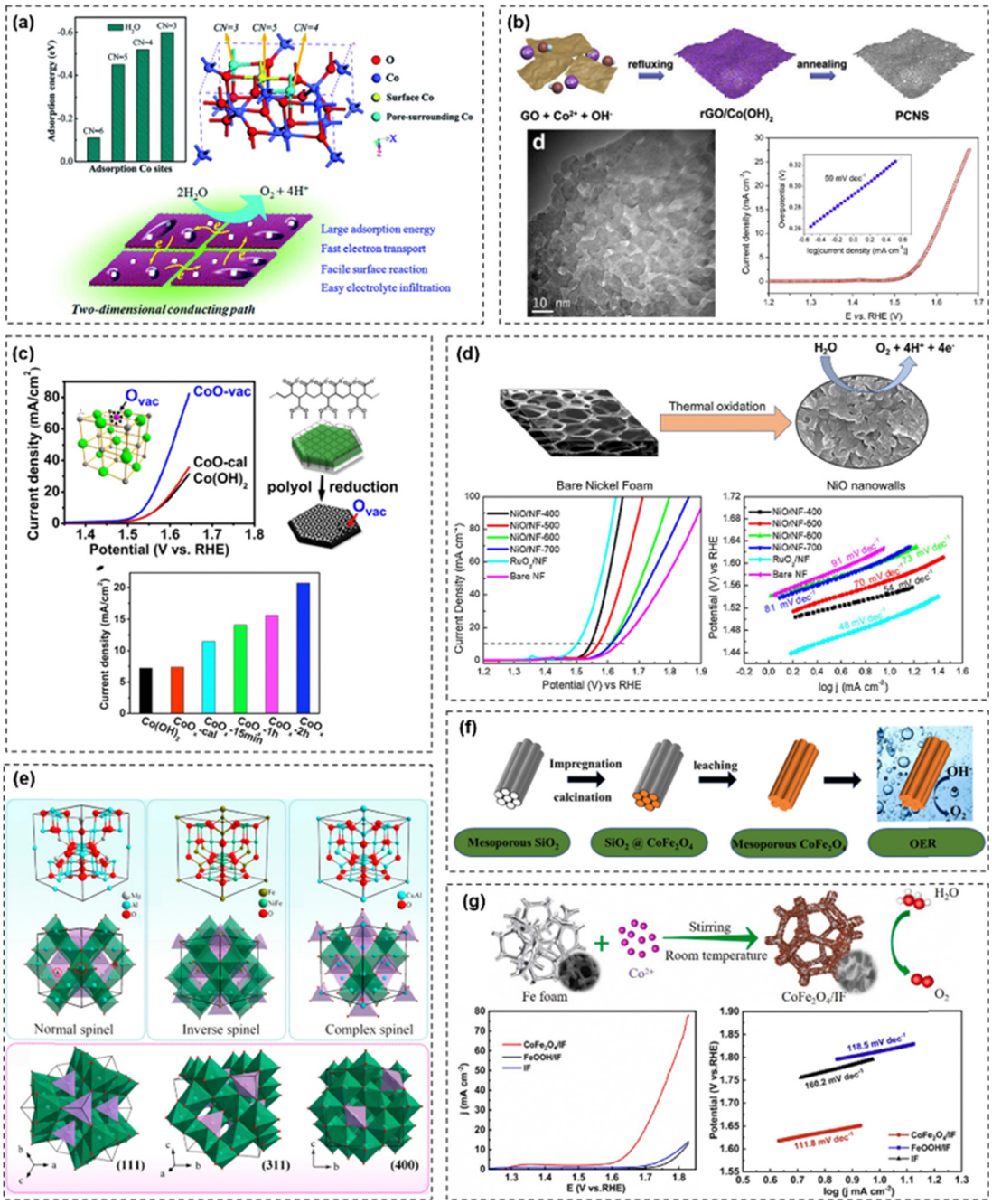

Fig. 4 Base metal oxide-based **OER** electrocatalysts: (a) characteristics of a porous Co_3O_4 nanosheet fabricated using a fast-heating strategy,[90] (b) schematic of the preparation of a porous Co_3O_4 nanosheet and linear sweep voltammetry (LSV) curves and Tafel slopes,[63] (c) schematic of the preparation of a porous CoO_x nanoplate with LSV curves,[68] (d) schematic of the preparation of a 3D porous NiO with LSV curves and Tafel slopes,[70] (e) representative structures of a normal spinel ($MgAl_2O_4$), an inverse spinel ($NiFe_2O_4$) and a complex spinel ($CuAl_2O_4$) in different styles and views,[92] (f) schematic of the preparation of $CoFe_2O_4$ through replication using a SBA-15 type mesoporous silica,[84] and (g) schematic of the preparation of a porous $CoFe_2O_4$ nanosheet with LSV curves and Tafel slopes.[93] Reproduced with permissions from ref. 90 and 92, Copyright 2014 and 2017 Royal Society of Chemistry and ref. 63, 68, 70, 84 and 93, Copyright 2016, 2018, 2018, 2019 and 2024 Elsevier.

converted $Co(OH)_2$ nanoplates to CoO_x with the formation of controllable oxygen vacancies (see Fig. 4c).[68] The $Co(OH)_2$ nanoplate was prepared by the hydrolysis of $CoCl_2$ and modified with polyacrylic acid as a reducing agent through the coordination of the carboxyl group to Co^{2+}. The resultant CoO_x nanoplate having surface oxygen vacancies showed an extremely small overpotential of 306 mV at 10 mA cm^{-2}. Lu *et al.* enhanced **OER** activity through the precise design of a highly porous Co_3O_4 replicated by using a KIT-6 type mesoporous silica with a doping of metal species (*e.g.*, Pd).[91] Electrons in Co^{3+} migrated due to the presence of Pd nanoparticles (NPs) and changed into Co^{4+} as the higher oxidation state, accelerating the formation of *OOH species. Accordingly,

the Pd-doped mesoporous Co_3O_4 type material showed an onset **OER** overpotential of 415 mV smaller than that without Pd (480 mV).

Pawar *et al.* designed a 3D porous NiO layer, which showed enough mechanical adhesion at the nickel (Ni) foam substrate surface by annealing at high temperatures (see Fig. 4d).[70] The thickness of the resultant nanoporous wall can be controlled by varying the annealing temperature. The parent porous structure of the Ni foam is important for the formation of a high-surface-area nanoporous structure. For example, the electrocatalyst constructed by the thinnest NiO porous layer on the Ni form showed an **OER** overpotential of 310 mV at 10 mA cm^{-2}.

The crystal structures of mixed metal oxides (spinel structure of AB_2O_4; A = Li, Mn, Zn, Cd, Co, Cu, Ni, Mg, Fe, Ca, Ge, Ba, *etc.* B = Al, Cr, Mn, Fe, Co, Ni, Ga, In, Mo, *etc.*) are determined as outlined by Bragg and Nishikawa since 1915.[94,95] Oxygen anions are arranged in a cubic close-packed lattice and metal ions fill the gaps between the tetrahedral and octahedral units (see Fig. 4e). The spinel is classified into three types, such as like normal, inverse and complex of crystal structures, depending on the cation distribution.[92] Such spinel-type mixed metal oxides are promising as high-performance **OER** electrocatalysts based on good conductivity, structural stability and high catalytic activity.[96] Fortunelli *et al.* demonstrated the importance of iron (Fe) species through theoretical calculation and experimental analysis, revealing that the lattice-oxygen oxidation mechanism proceeded in preference to the adsorbate evolution for **OER** using $CoFe_2O_4$.[97] Cuenya *et al.* also compared the **OER** activity based on epitaxially grown thin films of Co_3O_4(111), $CoFe_2O_4$(111) and Fe_3O_4(111).[98] $CoFe_2O_4$(111) showed up to about four and nine times activity than Co_3O_4(111) and Fe_3O_4(111), respectively. Hao *et al.* succeeded in fabricating an ordered mesoporous $CoFe_2O_4$ type material through hard-templating using an SBA-15 type ordered mesoporous silica (Fig. 4f).[84] This unique mesoporous $CoFe_2O_4$ type material resulted in not only an excellent **OER** overpotential of 342 mV at 10 mA cm^{-2} but also a high tolerance during **OER** even under alkaline conditions. Zhao *et al.* also prepared a porous $CoFe_2O_4$ nanosheet over Fe foam through a spontaneous redox reaction between the Fe foam and Co^{2+} (see Fig. 4g).[93] The resultant porous $CoFe_2O_4$ nanosheet showed a small **OER** overpotential of 429 mV at 10 mA cm^{-2} under neutral and alkaline conditions.

4.1.2. Base metal hydroxides. Base metal hydroxides are one of the most important compounds and are mainly divided into single-layered (SLH) and layered double hydroxides (LDH), depending on the number of metal species in the lattice. The crystal structures of SLH and LDH can be expressed by the general formulas such as $[M^{2+/3+}(OH)_{x-y}]_y^+[A^{n-}_{y/n}]_y \cdot mH_2O$ and $[M^{3+}_{1-x}M^{2+}_x(OH)_2]_x^+[A^{n-}_{x/n}]_x \cdot mH_2O$, respectively (see Fig. 5a). Such layered hydroxides have hierarchical porosity with high specific surface areas and facilitate the diffusion of water molecules as well as the release of gaseous products. Active site layers adjust the ordered arrangement and orientation of interlayer species by the strong electrostatic interactions between interlayer anions.[99–102] In particular, 3d transition metal (*e.g.*, Ni, Co and Fe) hydroxides exhibit adequate chemical bonding strength with catalytic reaction intermediates.[103] Since Hall disclosed in 1983 that α-$Ni(OH)_2$, one of the layered hydroxides, showed electrocatalytic **OER** activity,[104] a wide variety of base metal hydroxides (see Table 2) have been investigated as **OER** electrocatalysts. As disclosed in the cases using base metal oxides, the oxyhydroxide layer is the actual catalytic active site for **OER** and should be known in detail for developing electrochemical **OER** catalysts.

Abiti *et al.* synthesized a mesoporous cobalt hydroxide (*meso*-Co–OH) with a high specific surface area of 457 $m^2\ g^{-1}$ by a direct liquid crystal template method.[106] X-ray diffraction (XRD) measurement revealed that *meso*-Co–OH powder had the α-$Co(OH)_2$ structure and higher crystallinity than bulk Co–OH. The open mesoporous framework of *meso*-Co–OH significantly accelerated the mass property. A small overpotential of 320 mV at 25 mA cm^{-2} was observed by using *meso*-Co–OH, being 10 times lower than the current value of bulk $Co(OH)_2$ (see Fig. 5b). Lin *et al.* also reported the synthesis of α-$Co(OH)_2$ through the intercalation of NO_3^- into $Co(OH)_2$ and mixed β/γ-CoOOH through dehydration and dehydrogenation, and subsequent conversion to **OER**-active γ-$CoOOH_x$ and β-$CoOOH_y$ (see Fig. 5c).[107] *In situ* Raman spectra of α-$Co(OH)_2$, recorded as a function of the applied voltage, revealed that the metal species in the layered cobalt hydroxides were changed into those having a higher oxidation state during the **OER** reaction.

The chemical compositions of LDHs can be designed, and multiple metals have been evaluated to improve the **OER** performance. The combinations of trivalent (*e.g.*, Fe^{3+}) and divalent cations (*e.g.*, Co^{2+} and Ni^{2+}) significantly enhanced the **OER** activity by synergistic catalytic effects. Because Ni and Fe are on opposite sides of the volcano plot (see Fig. 5d),[108] the strength of chemical bonds between the active metal sites and reaction intermediates can be varied by mixing the metals. Accordingly, various types of NiFe-based **OER** catalysts have been developed so far. Duan *et al.* successfully deposited vertically aligned nanoplates of 3D porous NiFe-LDH over Ni foam by hydrothermal synthesis and accelerated the diffusion of electrolytes with a small **OER** overpotential of 280 mV at 30 mA cm^{-2} (Fig. 5e).[109] Additional doping of metals to NiFe-LDHs was also significant for enhancing the electronic conductivity related to **OER** activity.[132,133] Kim *et al.* reported a one-step electrochemical deposition of amorphous and 2D porous NiFeCo-LDH on Ni foam.[122] The elemental mapping images taken during observations by using transmission electron microscopy (TEM) revealed that NiFeCo LDH was almost fabricated with a stoichiometric atomic ratio of Ni : Fe : Co = 1 : 1 : 0.10 and the metals were distributed uniformly on the NiFeCo LDH nanosheet. The porosity of NiFeCo LDH also accelerated the electron transport and electrolyte diffusion. The amorphous structure of NiFeCo LDH is also interesting for intercalating OH^- and forming many edge sites and/or defects. The introduction of Co would cause a synergistic effect to show an excellent **OER** overpotential of 210 mV at 10 mA cm^{-2}.

4.1.3. Base metal phosphates. Base metal phosphates have drawn significant interest as ideal materials for high-efficiency energy conversion and storage applications based on high stability, utilization of earth-abundant metals, and unique

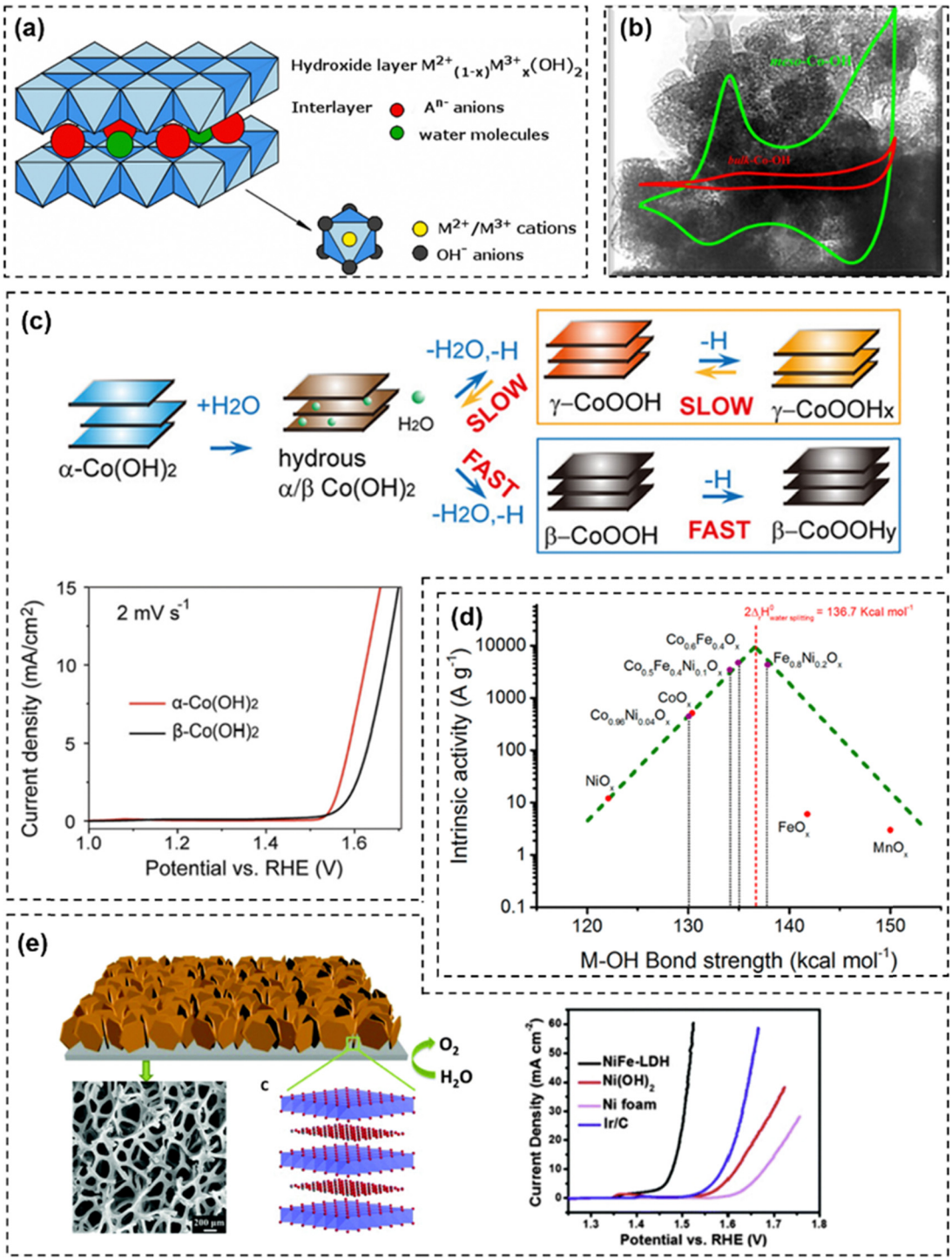

Fig. 5 Base metal hydroxide-based **OER** electrocatalysts: (a) schematic of layered double hydroxide,[105] (b) cyclic voltammetry at 50 mV s^{-1} in 1.0 M KOH solution of bulk-Co–OH and *meso*-Co–OH,[106] (c) schematic of the phase transition of $Co(OH)_2$ in the **OER** with LSV curves at a scan rate of 2 mV s^{-1} after the correction (*iR* compensation: 100%),[107] (d) volcano plot of the intrinsic activities of transition metal (oxy)hydroxides *vs.* M–OH bond strength where the green dotted lines indicate a hypothetical, perfect volcano,[108] and (e) schematic of the NiFe-LDH nanoplate with LSV curves.[109] Reproduced with permissions from ref. 105 and 106, Copyright 2019 and 2016 Elsevier, ref. 107 and 108, Copyright 2022 and 2016 American Chemical Society and ref. 109, Copyright 2014 Royal Society of Chemistry.

chemical and physical properties due to the presence of isolated and/or metal oxide-like clusters.[134,135] Base metal phosphates are preferentially built up to layered structures with open frameworks and thus exhibit electrochemical functions through the redox behavior of the various oxidation states of the metal species. The protons from the phosphate (P–OH)

Table 2 **OER** performance of the reported porous transition metal hydroxide-based **OER** catalysts

OER electrocatalyst	Substrate	Electrolyte	η_{10} (mV)	Tafel slope (mV dec^{-1})	BET surface area (m^2 g^{-1})	Pore size (nm)	Pore volume (cm^3 g^{-1})	Ref.
α-$Co(OH)_2$	Glassy carbon	1 M KOH	320 (η_{20})	—	457	4.0	0.43	106
β-$Co(OH)_2$	Co plate	1 M KOH	332	68	—	—	—	110
β-$Ni(OH)_2$	Ni foam	1 M KOH	250	61	—	—	—	111
$Co(OH)_2$@NCNTs	Ni foam	1 M KOH	270	72	—	—	—	112
Co-LDH	Glassy carbon	1 M KOH	218	88	103.82	13.9		113
CoFe-LDH	Glassy carbon	1 M KOH	410	111	127	<150	0.44	114
CoFe-LDH/BUGC	Biordered ultramicroporous graphitic carbon	1 M KOH	370	199	177	<16	0.33	114
CoFe-LDH/IMC	Immense microporous carbon	1 M KOH	305	85	251	<16	0.71	114
CoFe-LDH/MMC	Micro-/mesoporous carbon	1 M KOH	285	69	234	<20	0.83	114
NiFe LDH	Ni foam	0.1 M KOH	280 (η_{30})	50	0.24 (m^2 cm^{-2})	—	—	109
$Ni_{0.33}Fe_{0.66}$ DH	Glassy carbon	1 M KOH	320	59	429	2.0–10.0	0.54	115
$Ni_{0.5}Fe_{0.5}$ LDH	Glassy carbon	1 M KOH	284	48	414	2.0–10.0	0.72	115
$Ni_{0.66}Fe_{0.33}$ LDH	Glassy carbon	1 M KOH	248	46	333	2.0–4.0, 5.0–50	0.99	115
$Ni_{0.8}Fe_{0.2}$ LDH	Glassy carbon	1 M KOH	283	71	185	2.0–10.0	0.20	115
FeNi–OH LDH	Ni foam	1 M KOH	244 (η_{50})	47	—	—	—	116
NiCo LDH	Ni foam	0.1 M KOH	420	113	—	—	—	117
NiCo-LDH	Glassy carbon	1 M KOH	203	81	146.3	7.8	—	113
NiAl LDH	Ni foam	1 M KOH	180	93	—	—	—	118
NiFe LDH@NiCoP	Ni foam	1 M KOH	220	49	—	—	—	119
NiTe@FeNi LDH	Ni foam	1 M KOH	218	32	—	—	—	120
NiFeV LDH	Ni foam	1 M KOH	195 (η_{20})	42	—	—	—	121
NiFeCo LDH	Ni foam	1 M KOH	210	39	—	—	—	122
Ni_3S_2–NiFe LDH	Ni foam	1 M KOH	230 (η_{50})	61	—	—	—	123
NiFeCo-LDH@MXene	Ni foam	1 M KOH	220	52	—	—	—	124
FeOOH/Ni/NF	Ni foam	1 M KOH	190	26	30.4	200	—	125
$Co(OH)_2/La(OH)_3$	Carbon fiber paper	1 M KOH	273 (η_{100})	89	—	2.0	—	126
CuCoNi–OH	Carbon cloth	3 M KOH	290	58	33.1	>10	—	127
P–Ag–$Co(OH)_2$	Glassy carbon	1 M KOH	235	50	—	—	—	128
$Ni_{0.65}Mn_{0.35}$ LDH	Ni foam	1 M KOH	253 (η_{50})	130	—	—	—	129
Mo-NiO@NiFe LDH	Ni foam	1 M KOH	253 (η_{1000})	30	—	—	—	130
CoFe-LDH/MoS_2 @NDCDs	Ni foam	1 M KOH	258	93	12.4	39	0.13	131

groups can diffuse into the interlamellar space, contributing to good proton conductivity.[136] Nocera *et al.* reported that cobalt phosphate (CoPi) acted as excellent **OER** electrocatalysts under neutral and alkaline conditions.[137] The phosphate groups were stable during the catalytic reaction, acting as proton acceptors, and **OER** activity was enhanced by promoting the adsorption of water molecules with a distortion of the Co geometry and the electrochemical properties of base metal phosphates were strongly influenced;[138–141] the representative porous base metal phosphates are summarized in Table 3.

Yamauchi *et al.* prepared a crystalline CoPi-type material with a typical 2D hexagonal mesoporous structure using cetyltrimethylammonium bromide (CTAB, see Fig. 6a).[143] The abundant active sites were helpful for realizing an excellent **OER**

Table 3 **OER** performance of the reported porous transition metal phosphate-based **OER** catalysts

OER electrocatalyst	Substrate	Electrolyte	η_{10} (mV)	Tafel slope (mV dec^{-1})	BET surface area (m^2 g^{-1})	Pore size (nm)	Pore volume (cc g^{-1})	Ref.
CoPi film	Pt	0.1 M KOH	447	—	—	—	—	142
CoPi	Glassy carbon	1 M KOH	380	59	210	2.9	0.18	143
CoPi/Ti	Ti mesh	0.1 M PBS	450	187	—	—	—	144
$(Co_{0.5}Ni_{0.5})_3(PO_4)_2$	Ni foam	1 M KOH	273	59	—	—	—	145
CoPi-HSNPC	Glassy carbon	1 M KOH	320	85	69	—	—	146
$Ni_xCo_{3-x}(PO_4)_2$	Ni foam	1 M KOH	336	35	206	3.6	—	147
FeP–FeP_xO_y	Glassy carbon	1 M KOH	280	48	—	—	—	148
NFPy	Glassy carbon	1 M KOH	210	47	21.3	—	0.33	149
NiGLy	Carbon paper	1 M KOH	349	78	274	1.3	0.52	150
CoNTO-1–3	Carbon paper	1 M KOH	312	61	204	1.0	0.23	151
CoPIm	Carbon paper	1 M KOH	334	59	291	1.2	0.31	152
NiPIm	Carbon paper	1 M KOH	363	105	204	1.1	0.23	152
NiCoPIm	Carbon paper	1 M KOH	351	67	267	1.3	0.28	152
CoFePi	Glassy carbon	1 M KOH	277	31	170	12.3	0.70	153
CoFeNiPi	Glassy carbon	0.1 M KOH	309	51	—	—	—	153
CoNiPi	Glassy carbon	0.1 M KOH	402	87	80	2.0–50	—	153
FePi	Glassy carbon	0.1 M KOH	554	75	—	—	—	153

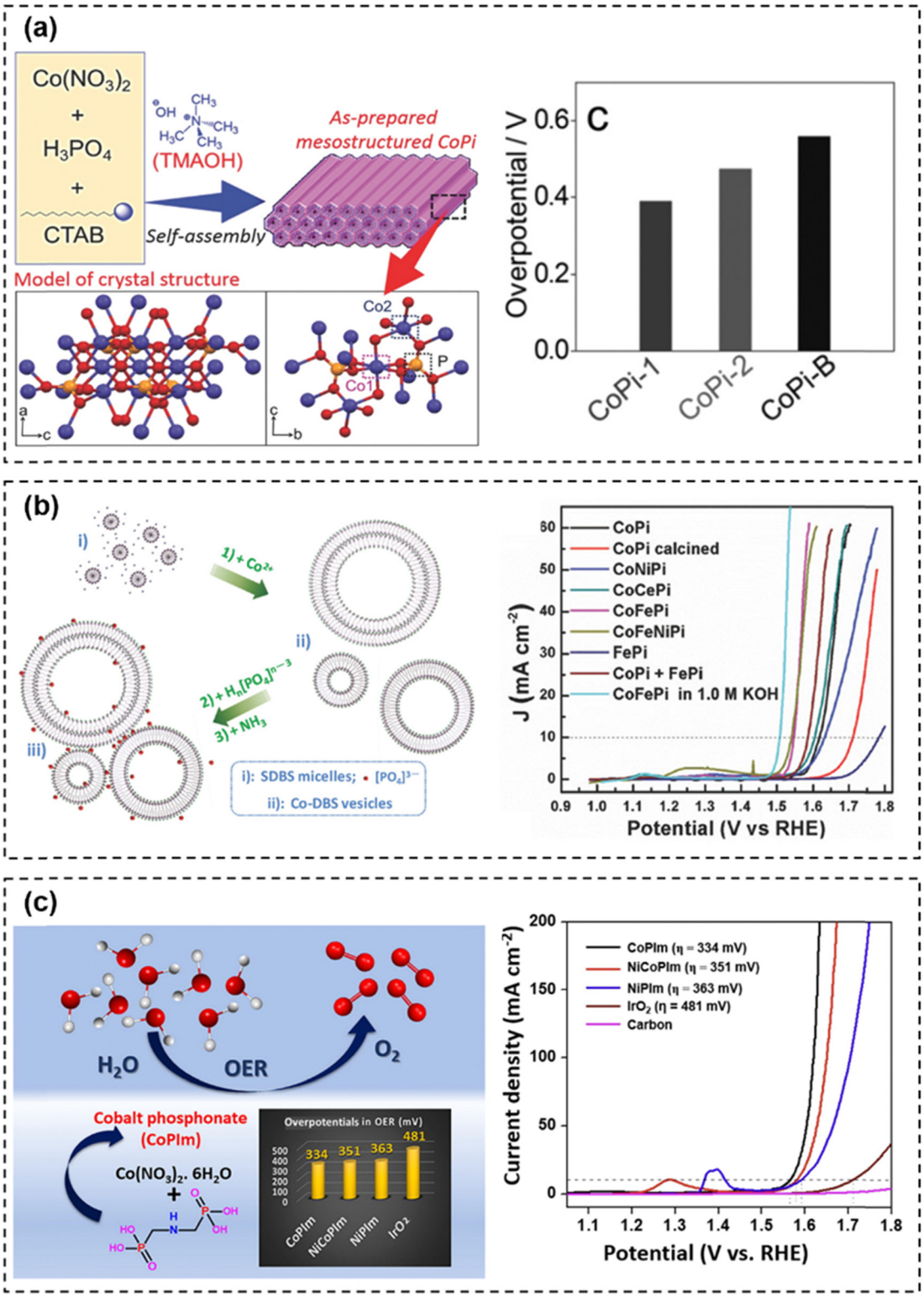

Fig. 6 Base metal phosphate-based **OER** electrocatalysts: (a) schematic of the preparation of CTAB templated CoPi with crystallized frameworks and the corresponding **OER** overpotentials,[143] (b) schematic formation mechanism of bi-templated CoPi and other transition metal containing ions and the resultant LSV curves at a scan rate of 10 mV s^{-1},[153] and (c) characteristics of organic–inorganic transition metal-based phosphonates synthesized through a simple hydrothermal reaction, and their LSV curves.[152] Reproduced with permissions from ref. 143 and 153, Copyright 2016 and 2018 Wiley-VCH and ref. 152, Copyright 2020 Elsevier.

overpotential of 380 mV at 10 mA cm^{-2}, being higher than that reported for the precious metal, base metal, and non-metal-based electrocatalysts and much higher than that observed for non-porous CoPi bulk (**OER** activity was 560 mV at 10 mA cm^{-2}).

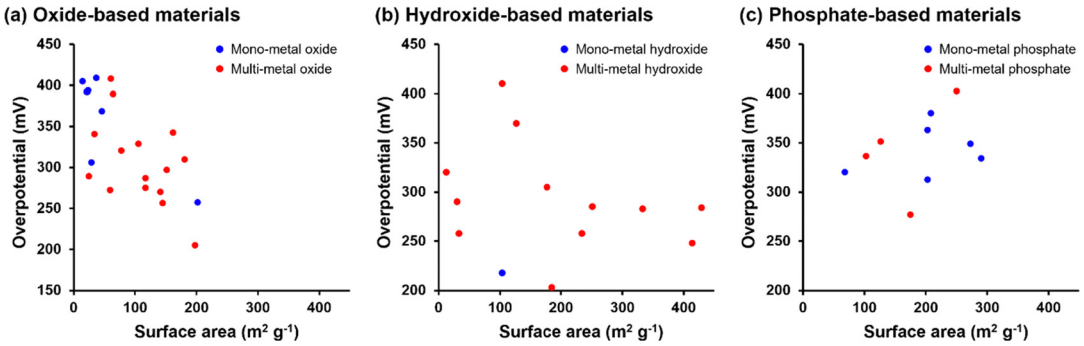

Fig. 7 Plots of the overpotential and BET-surface area in (a) oxide-based materials, (b) hydroxide-based materials, and (c) phosphate-based materials.

Accordingly, they demonstrated that the design of porous materials is quite important for enhancing **OER** activity. Besides, Zeng *et al.* focused on synergistic catalytic effects of trivalent Fe^{3+} and divalent Co^{2+} and Ni^{2+} for improving the electrochemical activity by adjusting the electronic environment of the active site.[153] Amorphous base metal phosphates, such as CoPi, FePi and binary CoFePi, were prepared by using a bi-template coprecipitation method and the resultant **OER** activities were compared (see Fig. 6b). By the synergistic effects, the **OER** overpotential CoFePi (315 mV at 10 mA cm^{-2}) was quite superior to those observed for (388 mV and 554 mV). To demonstrate a new guideline for the design of base metal phosphates to improve **OER** performance, Yamauchi *et al.* also synthesized three porous metal phosphonates such as cobalt (CoPIm), nickel (NiPIm) and nickel–cobalt phosphonates (NiCoPIm) by utilizing iminodi(methylphosphonic acid) that can interact with Co^{2+} and Ni^{2+} with the introduction of organic functions (see Fig. 6c).[152] An electron donation from nitrogen filled the M–OH antibonding orbital and caused modulation of the interactions between metal and oxygen, leading to excellent **OER** overpotentials of 334 mV (CoPIm), 363 mV (NiPIm) and 351 mV (NiCoPIm).

The morphological design of porous metal phosphates has also been achieved by various methods. The strong proton donation property from the phosphate group is helpful for overcoming the low conductivity that has been a problem in the cases of base metal oxides. In addition, considering the synthesis pathway of metal phosphonates, a wide variety of metal phosphonates, where metal phosphate units and organic groups are located at the molecular scale in the inorganic–organic hybrid frameworks, are prepared with the selection of metal species and the design of organic functions.[154,155] This unique structural feature is different from those of inorganic-only materials. The introduction of organic groups gives us a good opportunity to tune the electronic structure of the active metal species as an environment optimized for **OER**.[153]

In base metal-based inorganic materials, forming porous nanostructures is the most efficient and universal strategy to enhance **OER** activity. As summarized in Fig. 7, a certain correlation between the specific surface area and **OER** performance was confirmed for oxide-based materials, though such a tendency has hardly been found for hydroxide- and phosphate-based ones. However, it has been reported that porous materials of hydroxides and phosphates show higher **OER** performance than non-porous ones.[106,143] Accordingly, making inorganic-based electrocatalysts more porous and promoting mass transport have been effective ways to improve their **OER** performance. The precise control of porous structures (*e.g.*, templating to control the uniformity of pore) is also very important for understanding the effects of pore size on inorganic-based porous **OER** electrocatalysts.

In recent years, further optimization of **OER** activity has been investigated not only by improving the physical properties but also by adjusting the electronic environment of metal species through the combination of multiple metal species and the doping of heteroatoms such as nitrogen and sulfur. Synergistic catalytic effects between trivalent Fe ions and divalent Co or Ni ions also play an important role in enhancing the **OER** activity. Metal composite materials containing multiple metal species are up-and-coming candidates for designing highly active electrocatalysts (see Fig. 8). The lack of precise elucidation of the active site structure and **OER** mechanism is a common and major problem in the case of base metal-based electrocatalysts. Recent developments in *operando* and *in situ* spectroscopic technologies have revealed that the **OER** mechanism varies according to the catalyst and changes in the reaction environment.[156] The diversity of the **OER** mechanism is an obstacle to designing electrode materials for scale-up to industrial applications. More detailed and accurate elucidation of the **OER** mechanism is urgently needed to systematically understand the influences of the electronic states in the structures and metal species on the **OER** performance.

4.2. Organic–inorganic hybrid OER electrocatalysts

4.2.1. Conductive sites in MOFs. MOF is constructed through the coordination between inorganic metal complexes and organic linkers and the well-defined crystalline structure of MOF allows us to evaluate the **OER** performance. However, the use of MOFs is quite limited as electrocatalysts due to their poor electronic conductivity. By improving the electronic conductivity arising from organic linkers, electron-conducting and proton-conducting MOFs have great potential to act as **OER** electrocatalysts without additional cost. Representative MOFs for **OER** are summarized in Table 4.

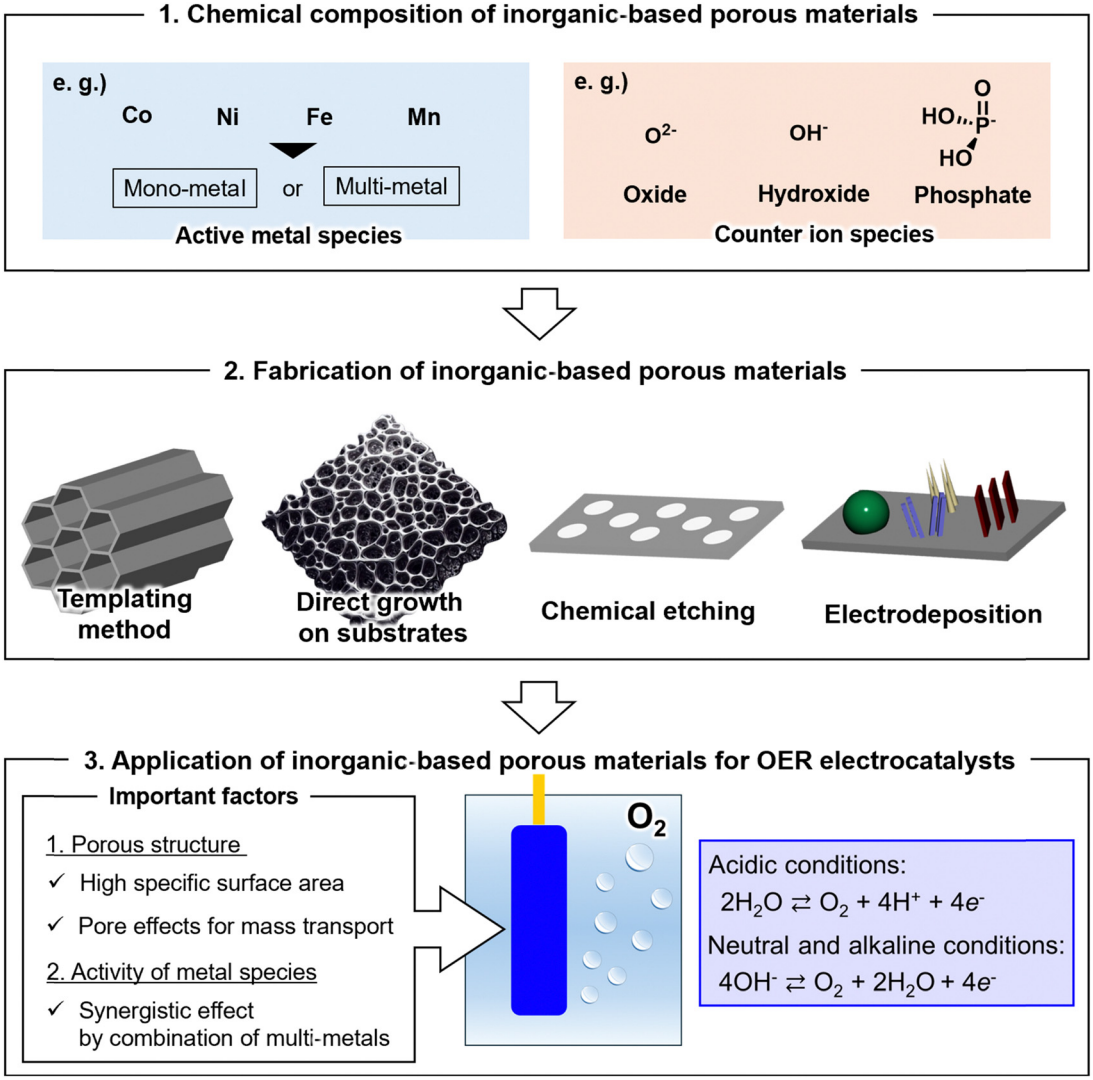

Fig. 8 Schematic technical diagram of inorganic-based porous **OER** electrocatalysts.

Su *et al.* fabricated MOFs with different conductivities due to a modulation of the electronic active site by substituting metal species and linkers in the conductive MOF.[173] The conductivity was correlated with the **OER** activity because an enhancement in the conductivity promotes the transfer and the supply of electrons during the reactions. Du *et al.* synthesized a nickel phthalocyanine-based 2D MOF (NiPc-MOF) on fluorine-doped tin oxide (FTO) substrate (see Fig. 9a).[166] NiPc-MOF promoted an electron transfer within the structure *via* in-plane π-delocalization and weak out-of-plane π–π stacking of phthalocyanine, resulting in a small **OER** overpotential of 250 mV at 1.0 mA cm^{-2}. The triphenylene derivative organic linker is very interesting for adjusting the electronic conductivity in the range of 10^{-6} to 10^{1} S cm^{-1} by designing the organic linker and the valuation of the metal centers.[174–178] Wang *et al.* succeeded in synthesizing a nanowire array of triphenylene derivative 2D MOF (Fe_1Ni_4–HHTP, HHTP = 2,3,6,7,10,11-hexahydroxytriphenylene) on a carbon cloth (CC) substrate (see Fig. 9b).[167] Calculations based on the density functional theory (DFT) revealed that self-adaptive structural adjustment of the Fe site was generated through the hydrogen bond between the **OER** intermediate and the adjacent layer with the reduction of the free energy in the **OER** process. The resultant Fe_1Ni_4–HHTP showed small **OER** overpotentials of 213 mV and 300 mV at 10 mA cm^{-2} and 150 mA cm^{-2}, respectively. Zhang *et al.* synthesized two isostructural MOFs with different proton conductivities (FJU-82-Co; 7.40 × 10^{-5} S cm^{-1}, FJU-82-Zn; 5.80 × 10^{-7} S cm^{-1} at 60 °C under 98% RH) to elucidate a direct correlation between proton conductivity and **OER** activity (see Fig. 9c).[179] FJU-82-Co showed a much lower overpotential of 570 mV than that observed for FJU-82-Zn (1170 mV) at 1.0 mA cm^{-2}. Jiao *et al.* encapsulated 3-hydroxy-2,5,6,8,9-pentanitro-pyrene-1-sulfonate (HPTS) as a dye molecule into the pores of a MOF (dye@MOF) (see Fig. 9d).[168] The hydroxyl and sulfonic groups of the HPTS molecule improved the proton conductivity of dye@MOF. The resultant dye@MOF showed an extremely small **OER** overpotential of 194 mV at 10 mA cm^{-2} and higher **OER** activity.

4.2.2. Function modified MOFs. In addition to using conductive organic molecules as the organic linker and the

Table 4 **OER** performance of the reported porous transition metal phosphate-based **OER** catalysts

OER electrocatalyst	Substrate	Electrolyte	η_{10} (mV)	Tafel slope (mV dec^{-1})	BET surface area (m^2 g^{-1})	Pore size (nm)	Pore volume (cc g^{-1})	Ref.
NiCoFe-MOF-400 °C-1 h	Glassy carbon	1 M KOH	238	29	558	1	0.19	157
NiCoFe-MOF-74-600 °C-2 h	Glassy carbon	1 M KOH	366	117	197	—	0.060	157
(Co,0.3Ni)-HMT	Glassy carbon	1 M KOH	330	66	100.2	18.4	0.54	158
Ni(Fe)-MOF-74	Ketjenblack	1 M KOH	274	40.4	684	1.0, 5.0	0.34	159
NiFe-MOF/G	Glassy carbon	1 M KOH	258	49	437	—	—	160
FeNi-DOBDC-3	Carbon	1 M KOH	270 (η_{50})	62.7	77.9	11.0	0.27	161
MFN@GA/NF	Ni foam	1 M KOH	270 (η_{20})	66	77.8	12.4	—	162
FCN-BTC-MOF	Ni foam	1 M KOH	218	29.3	233.9	3.3	—	163
NiCo-MOF	Glassy carbon	1 M KOH	270	—	27.5	1.5–60	—	164
$Co_xZn_{3-x}(HITP)_2$	Glassy carbon	1 M KOH	210	50	520.5	0.71	0.60	165
$Co_xMn_{3-x}(HITP)_2$	Glassy carbon	1 M KOH	250	54	371.5	0.53	0.45	165
$Co_xNi_{3-x}(HITP)_2$	Glassy carbon	1 M KOH	280	56	403.0	0.74	0.50	165
NiPc-MOF	Quartz	1 M KOH	250 (η_{onset})	74	593	—	—	166
Fe_1Ni_4–HHTP	Carbon cloth	1 M KOH	213	96	—	1.8	—	167
dye@MOF	Ni foam	1 M KOH	194	199	—	—	—	168
$Co_3(HITP)_2$	Carbon cloth	1 M KOH	254	86.5	281	—	0.62	169
Am-FeCo(OH)$_x$-30	Glassy carbon	1 M KOH	257	47	838	2.0	—	170
RuNC/Ni-M-SH	Glassy carbon	1 M KOH	248	57.3	420	1.41	—	171
MOF-H	Ni foam	1 M KOH	263	63.4	—	—	—	172
MOF-F	Ni foam	1 M KOH	262	52.7	—	—	—	172
MOF-Cl	Ni foam	1 M KOH	258	57.5	—	—	—	172
MOF-Br	Ni foam	1 M KOH	251	44.5	—	—	—	172

encapsulation of conductive organic molecules into the pores, electron-donating organic linkers improve **OER** activity with the design of functional groups.[170,171,180] The electronic structure of the active site can be tuned by the interaction between substituents and metal species, revealing that the functional design of MOFs is helpful for understanding the electronic effects of active metal species in **OER** reactions under optimal conditions.

Jia *et al.* succeeded in fabricating a defect-rich hierarchical Am–FeCo(OH)$_x$ hybrid architecture by using amino-functionalized iron-based MOF (MIL-101) as a sacrificing modification agent (see Fig. 10a).[170] The resultant hierarchical 3D architecture with abundant active sites/defects and coordinated unsaturated sites reduced the reaction energy barrier and accelerated the reaction kinetics, leading to a small **OER** overpotential of 257 mV at 10 mA cm^{-2}. The enhanced surface hydrophilicity also promotes the release of oxygen (O_2) bubbles and proton-coupled electron transfer. Li *et al.* synthesized MIL-101(Fe)-X with the different amounts of the amino (–NH_2) group (X = H : NH_2 = 1 : 0, 1 : 0.5, 1 : 1, 1 : 2, 1 : 4, 0 : 1, specific surface area; 380 m^2 g^{-1} at the highest) by the solvothermal synthesis (see Fig. 10b).[180] The generated electron–hole pairs were effectively separated by the incorporation of the electron-donating –NH_2 group, and the oxygen evolution rate was maximized at the ratio of H : NH_2 = 1 : 2 under simulated sunlight irradiation of 11.7 mmol h^{-1} g^{-1}. An excessive introduction of the –NH_2 group resulted in the reduction of the **OER** activity with a decrease in the porosity. Tripathi *et al.* synthesized a thiol (–SH) functionalized MOF (Ni–M–SH) by the solvothermal reaction of Ni nodes and thiolated 2-aminoterephthalic acid (TPA-SH), followed by the adsorption of ruthenium (Ru) ions to obtain RuNC/Ni–M–SH (see Fig. 10c).[171] Because the –SH group was helpful for electron transfer and oxidation of Ni offered electrons, Ru^{3+} was stabilized in the RuNC/Ni–M–SH based electrocatalyst showing a small overpotential of 248 mV at 10 mA cm^{-2}.

The **OER** performance is not explained systematically by using the porosity of MOF type materials only. However, by preparing a series of porous electrodes with different surface areas from a MOF-type material, a higher specific surface area is useful for improving the **OER** activity.[157] Thus, increasing the surface area as much as possible is an important factor for maximizing the **OER** performance. In terms of the pore size, although the resultant data are confusing while using the difference in the composition of MOF-type materials, small pores having a diameter of around 1–3 nm seem to be suitable for **OER** because reactants/products are very small (<0.5 nm) such as water, hydroxide ions and oxygen atoms.

Organic–inorganic hybrid MOF-type materials have attracted much attention in the field of electrocatalysis with the outstanding development of synthetic strategies (see Fig. 11). Conductive MOFs, including conductive organic components, have been developed and several studies have revealed that the electron/proton conductivity of the frameworks is helpful for improving the **OER** performance. The functional design of organic linkers is an important strategy to improve the **OER** activity. To maximize the **OER** activity of MOF-based electrocatalysts, a comprehensive study should be conducted for understanding the effects of porous structure, active metal center and organic linker. The development of a scalable and cost-effective synthesis method is also essential for their industrial use.

4.3. Organic OER electrocatalysts

All frameworks of COF-based materials are constructed by organic molecules, with the further potential for improving the electron conductivity by tuning the porosity. However, COF has not been investigated as electrocatalysts because it does not have active sites like the metal species of MOF-based materials. Accordingly, COF without the active metal site needs the control of the local electronic environment by doping

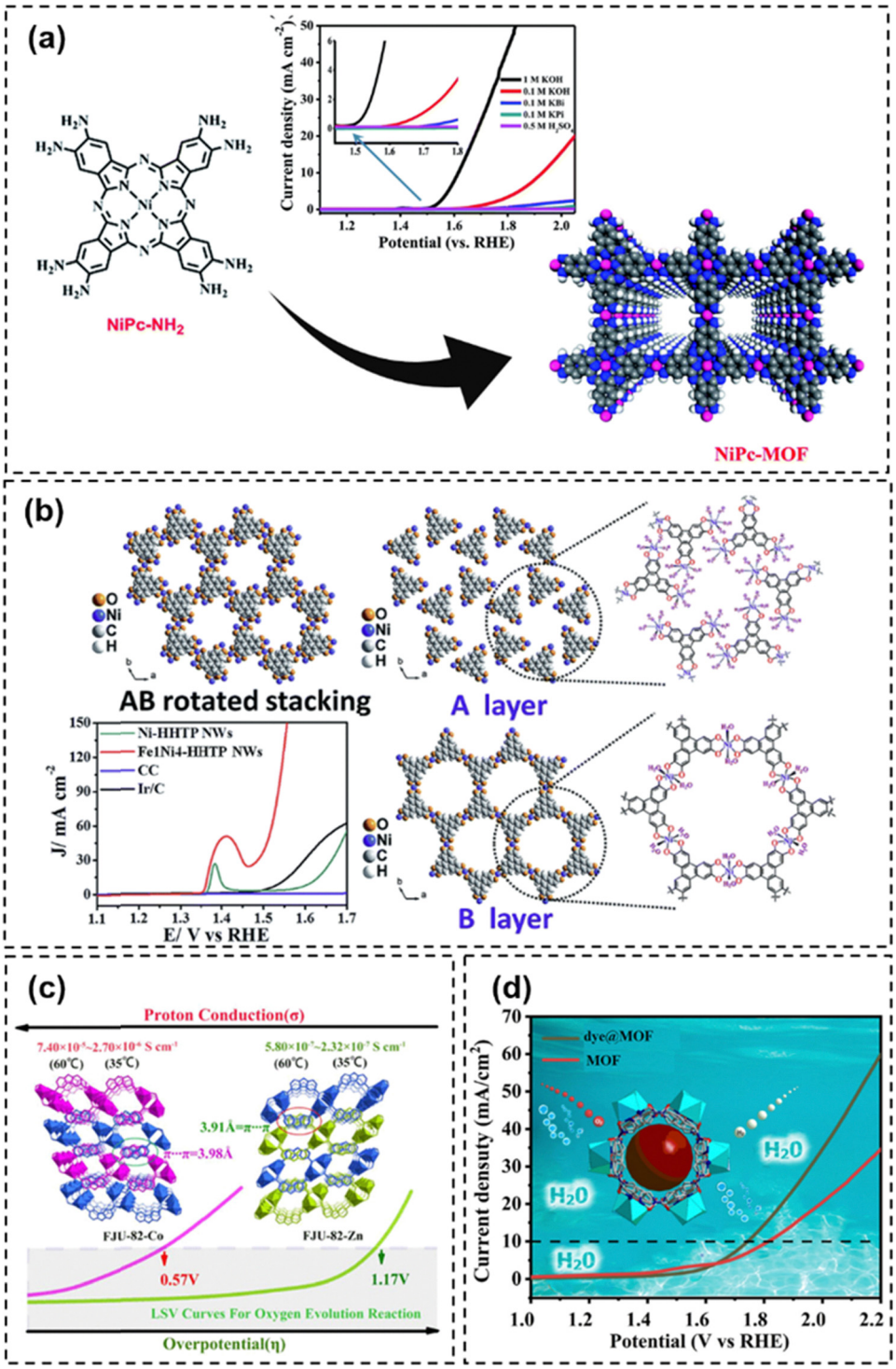

Fig. 9 Conductive site introduced MOF-based **OER** electrocatalysts: (a) schematic of the preparation of NiPc-MOF and LSV curves in various electrolytes,[166] (b) space-filling drawings of Ni-HHTP along the *c* axis with resultant LSV curves in 1 M KOH,[167] (c) perspective view of the four-layer stacking diagram along the *b*-axis of FJU-82-Co and FJU-82-Zn,[179] and (d) LSV curves of dye@MOF.[168] Reproduced with permissions from ref. 166 and 167, Copyright 2018 and 2019 Royal Society of Chemistry, ref. 179, Copyright 2020 American Chemical Society and ref. 168, Elsevier, Copyright 2023.

heteroatoms to improve electrocatalytic activity.[181] In this strategy, active metal species can be introduced at a desired location by designing the molecular structure of the organic monomer. Such COFs play an extremely vital role in elucidating the **OER** mechanism at the active site in combination with completely crystallized porous structures. Representative COFs for **OER** are summarized in Table 5. Kurungot *et al.* synthesized a COF (TpBpy) with a bipyridine moiety by the Schiff base reaction of 1,3,5-triformylphloroglucinol (Tp) and 2,2′-bipyridine-5,5′-diamine (Bpy) and then coordinated Co^{2+} with

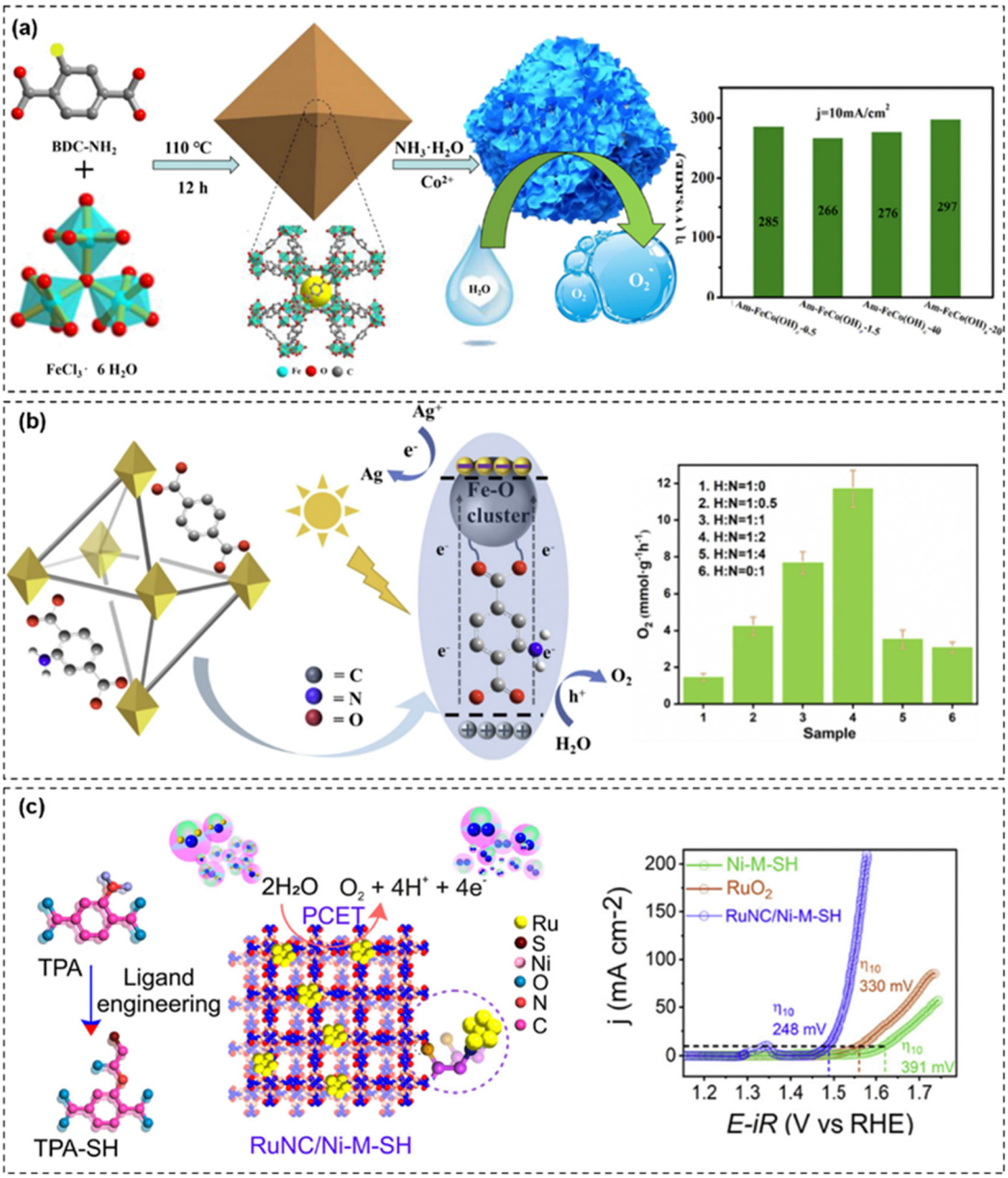

Fig. 10 Function modified MOF based **OER** electrocatalysts: (a) schematic of the preparation of Am–FeCo(OH)$_x$ and the comparison of overpotentials at 10 mA cm^{-2} with different reaction times,[170] (b) photocatalytic oxygen evolution mechanism of MIL-101(Fe)-X with the comparison of O_2 evolution rates with the increase in amino group content,[180] and (c) schematic of the preparation of RuNC/Ni–M–SH and LSV curves at a scan rate of 0.001 mV s^{-1} in O_2-saturated 1 M KOH.[171] Reproduced with permissions from ref. 170 and 180, Copyright 2021 and 2024 Elsevier and ref. 171, Copyright 2024 American Chemical Society.

the bipyridine moiety to fabricate Co-TpBpy with abundant Co–N active sites (see Fig. 12a).[182] The composite COF showed an **OER** overpotential of 400 mV at 1.0 mA cm^{-2} under neutral pH conditions. Chen *et al.* synthesized another COF (Co-PDY) using a porphyrin derivative (5,10,15,20-(tetra-4-ethynylphenyl)-porphyrin; Co-TEPP) with central coordination of Co^{2+} (see Fig. 12b).[183] The stable Co–N_4 sites were distributed throughout the 2D plane of Co-PDY and served as highly active centers, leading to a small overpotential of 270 mV at 10 mA cm^{-2}. Other heterocyclic compound derivatives, such as pyrimidine, triazole, and triazine, can also be used as organic monomers of COF to design active metal species.[184–186]

Even in COF, the specific surface area is not the same as the number of active sites related to the **OER** performance. The design of coordination sites and the pore volume is important for increasing active sites because the active metal species are coordinated in the frameworks of COF-based electrocatalysts after the formation of periodic porous structures. In addition, the pore size of COF-based electrocatalysts seems to be slightly larger than that of MOF-based ones. This is due to the fact that

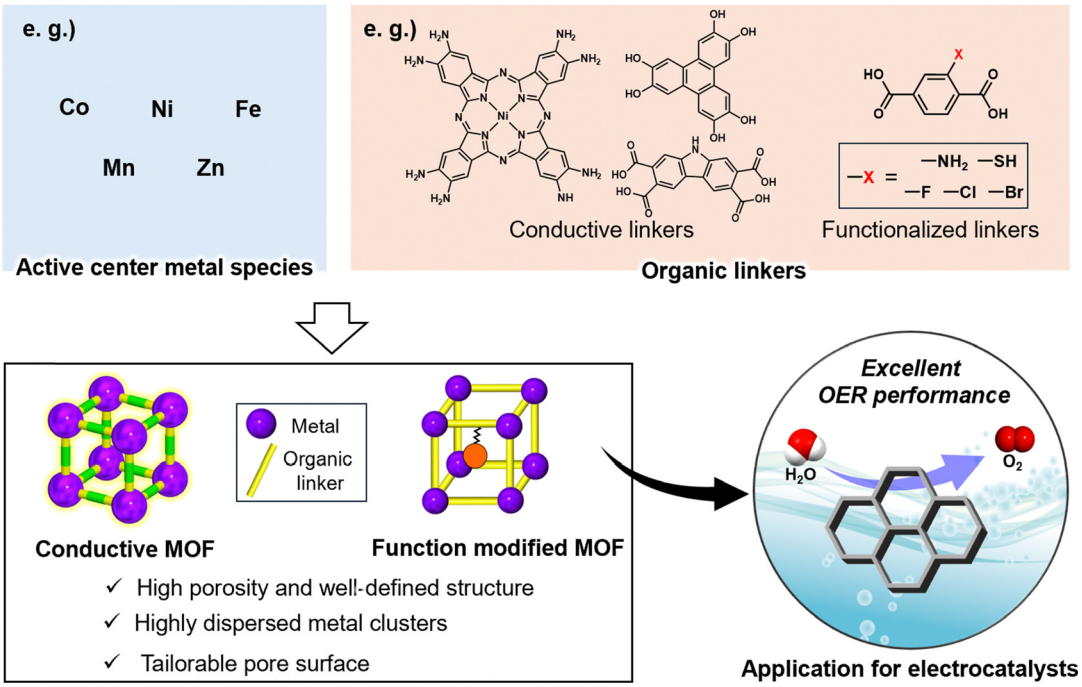

Fig. 11 Schematic technical diagram of MOF-based **OER** electrocatalysts.

Table 5 **OER** performance of the reported porous transition metal hydroxide-based **OER** catalysts

OER electrocatalyst	Substrate	Electrolyte	η_{10} (mV)	Tafel slope (mV dec^{-1})	BET surface area (m^2 g^{-1})	Pore size (nm)	Pore volume (cm^3 g^{-1})	Ref.
Co-TpBpy	Glassy carbon	0.1 M phosphate buffer (pH 7)	400 (η_1)	59	450	—	—	182
Co-PDY	Cu foam	1 M KOH	270	99	—	2.3	—	183
Co@COF-Pyr	Glassy carbon	1 M KOH	450	100	392	1.6	0.37	184
COF-TpDb-TZ-Co	Glassy carbon	1 M KOH	390	82	241	1.4	—	185
Ni-COF	Carbon cloth	1 M KOH	302	56	—	—	—	186

reactants and products should have access to active metal centers.

In the application of COF for **OER**, the recent trend is the introduction of active metal species with the design of organic monomers (see Fig. 13), providing a flexible control of active metal species. In combination with the clear structure of COF-based porous materials, it is expected to make a significant contribution to the elucidation of the **OER** mechanism at the active site. The limited number of monomer candidates and the small variation in porous structure are major problems. The field of applications of COF as electrochemical catalysis is just beginning to attract attention, and further development is desirable.

5. Recent trends for developing OER electrocatalysts

5.1. Bifunctional electrocatalysts

Since the discovery of a cobalt-oxo/hydroxo-phosphate layer-coated metallic cobalt bifunctional for **HER** and **OER** by Cobo *et al.* in 2012,[187] the development of **HER-OER** bifunctional electrocatalysts has been one of the research topics to solve the process cost and cross-contamination issue by the elution of two electrodes. As summarized in Table 6, the design of such unique electrocatalysts is quite complicated because surface conditions are different during **HER** and **OER** reactions.[188] Guan *et al.* synthesized $CoFe_2O_4$ on Ni foam hydrothermally, followed by the electrodeposition of CoNi nanosheets (see Fig. 14a).[189] A nanoarchitectured CoNi/$CoFe_2O_4$/NF showed small **HER** and **OER** overpotentials of 82 mV and 270 mV at 10 mA cm^{-2}, respectively. The overall water-splitting reaction in 1 M KOH for the cathode and the anode reached the current densities of 10 mA cm^{-2} and 100 mA cm^{-2} by small cell voltages of 1.57 V and 1.75 V, respectively. Ren *et al.* succeeded in fabricating a bifunctional electrocatalyst (FeP/Ni_2P) through the hybridization of iron and dinickel phosphide on Ni foam.[190] The resultant porous FeP/Ni_2P showed excellent overpotentials of 14 mV and 154 mV at 10 mA cm^{-2} in 1 M KOH for **HER** and **OER**, respectively, being comparable to those of Pt (57 mV) and IrO_2 (300 mV) as the benchmarks for **HER** and **OER**. The overall water-splitting reaction in 1 M KOH for the cathode and the anode reached a current density of 10 mA cm^{-2}

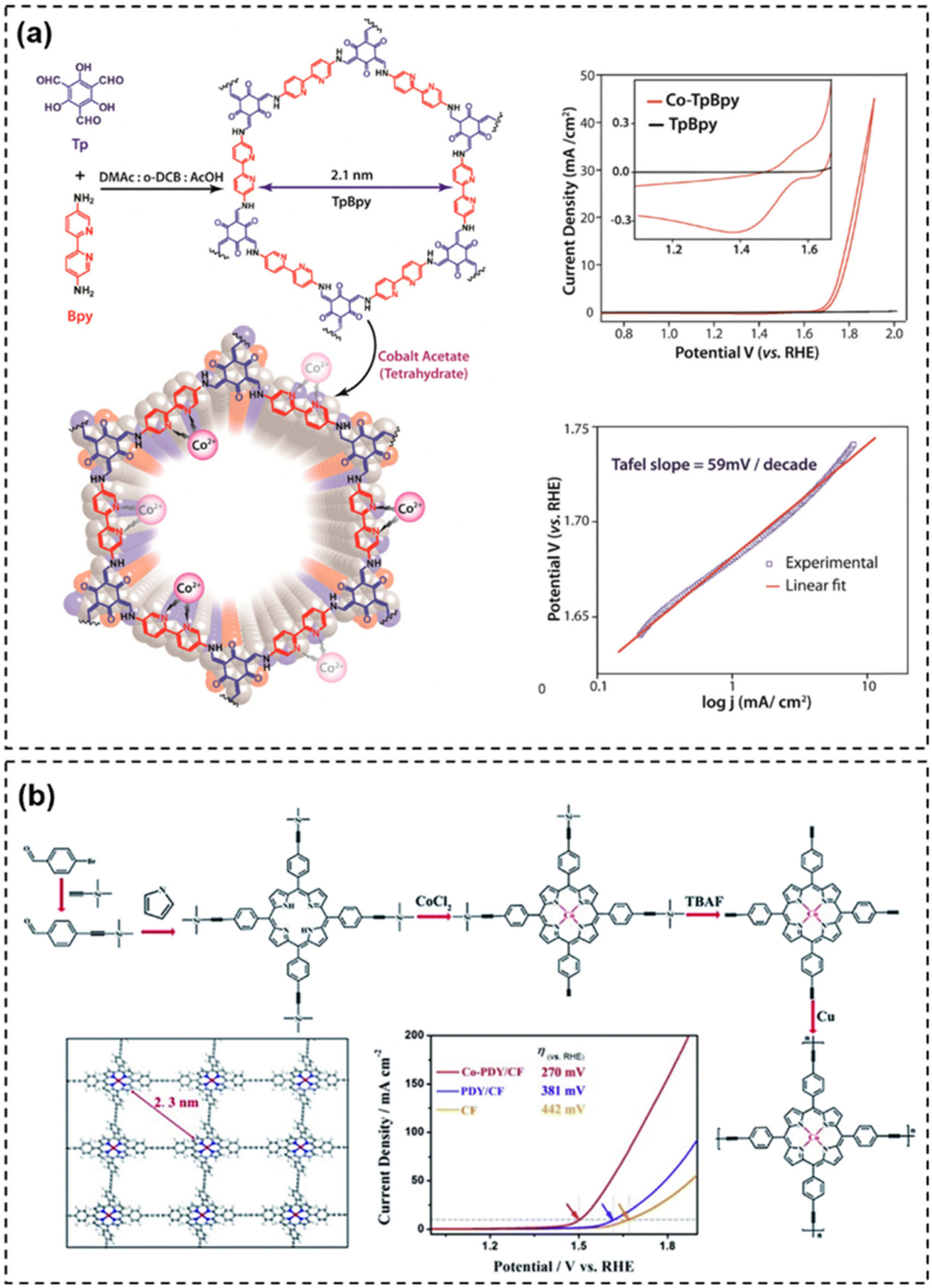

Fig. 12 Active site designed COF-based **OER** electrocatalysts: Schematic routes to synthesize (a) Co-TpBpy *via* proton tautomerized Schiff base condensation and Co^{2+} impregnation with cyclic voltammogram and Tafel plot in a phosphate buffer at pH = 7.0[182] and (b) Co-PDY with LSV curves.[183] Reproduced with permissions from ref. 182 and 183, Copyright 2016 and 2019, with permission from the Royal Society of Chemistry.

by a small cell voltage of 1.42 V, being lower than that observed for the benchmark catalysts (1.57 V for IrO_2–Pt).

Liu *et al.* succeeded in fabricating an outstanding bifunctional electrocatalyst FeNiZn/$FeNi_3$@NiFe (see Fig. 14b).[204] The interfaces between FeNiZn and $FeNi_3$ were active for the reactions, which were promoted due to fast mass transport by the multimodal porous structure. The excellent electrocatalytic activity was then achieved even at the high current density

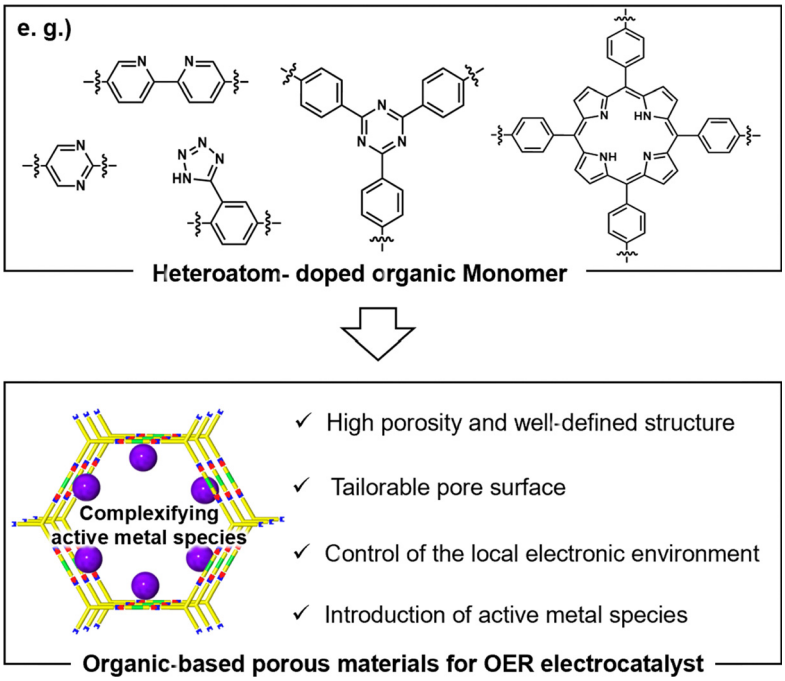

Fig. 13 Schematic technical diagram of COF-based **OER** electrocatalysts.

(1000 mA cm^{-2}) with small overpotentials of 367 mV and 245 mV in 1 M KOH for both **HER** and **OER**, respectively. Besides, FeNiZn/$FeNi_3$@NiFe could operate for 400 hours at 1000 mA cm^{-1} without significant deactivation. Kim *et al.* developed N-self-doped defect-rich porous carbon nanosheets derived from *Platycladus orientalis* tree-cone biomass as a carbon-based bifunctional electrocatalyst without metals (see Fig. 14c).[206] This nanosheet-type material exhibited an exceptional specific surface area of 3369 m^2 g^{-1}, pore volume of 2.1 cm^3, and electric conductivity of 12.69 S cm^{-1} and thus showed small

Table 6 Performance of the reported bifunctional porous electrocatalysts for the **HER** and **OER**

			HER		**OER**				
Electrocatalyst	Substrate	Electrolyte	η (mV)	Tafel slope (mV dec^{-1})	η (mV)	Tafel slope (mV dec^{-1})	Cell voltage (V at 10 mA cm^{-2})	Long-term stability	Ref.
PCPTF	Glass slide	1 M KOH	430 (η_{30})	53	330 (η_{30})	65	—	13.8 h (at 10 mA cm^{-2})	191
NSP-Co_3FeN_x	Ni foam	1 M KOH	23 (η_{10})	94	222 (η_{20})	46	1.54	2000 CV cycle	192
Cu-CMP	Glassy carbon	1 M KOH	350 (η_{10})	135	450 (η_{10})	62	—	12 h (at 1 mA cm^{-2})	193
Ni/NiP	—	1 M KOH	130 (η_{10})	59	270 (η_{30})	73	1.61	4 h (at 10 mA cm^{-2})	194
MoO_2	Ni foam	1 M KOH	27 (η_{10})	41	260 (η_{10})	54	1.53	24 h (at 10 mA cm^{-2})	195
Ni_2P/Ni	Ni foam	1 M KOH	98 (η_{10})	72	200 (η_{10})	—	1.49	20 h (at 20 mA cm^{-2})	196
NiFe/$NiCo_2O_4$	Ni foam	1 M KOH	105 (η_{10})	88	340 (η_{1200})	39	1.67	20 h (at 10 mA cm^{-2})	197
FeP/Ni_2P	Ni foam	1 M KOH	14 (η_{10})	24	154 (η_{10})	23	1.42	40 h (at 500 mA cm^{-2})	190
Fe-H_2cat	Fe foam	1 M KOH	243 (η_{10})	77	238 (η_{10})	83	1.65	50 h (at 10 mA cm^{-2})	198
$Ni_{0.75}Fe_{0.125}V_{0.125}$-LDHs/NF	Ni foam	1 M KOH	125 (η_{10})	64	231 (η_{10})	39	1.59	15 h (at 30 mA cm^{-2})	199
CoNi/$CoFe_2O_4$	Ni foam	1 M KOH	82 (η_{10})	96	230 (η_{10})	45	1.57	48 h (at 100 mA cm^{-2})	189
NiFeCo LDH	Ni foam	1 M KOH	108 (η_{10})	73	210 (η_{10})	39	1.57	50 h (at 10 mA cm^{-2})	122
CoP–N	Co foam	1 M KOH	100 (η_{50})	82	260 (η_{50})	51	1.61	50 h (at 50 mA cm^{-2})	200
Ni@NiFe LDH	Ni foam	1 M KOH	92 (η_{10})	72	218 (η_{10})	66	1.53	24 h (at 10 mA cm^{-2})	201
$Co_3(OH)_2(HPO_4)_2$	Ni foam	1 M KOH	87 (η_{10})	91	182 (η_{10})	69	1.54	240 h (at 30 mA cm^{-2})	202
Ni–Co–Fe–P NBs	Ni foam	1 M KOH	35 (η_{10})	65	187 (η_{10})	29	1.46	100 h (at 100 mA cm^{-2})	203
FeNiZn/FeNi3 @NiFe	Ni foam	1 M FeKOH	245 (η_{1000})	45	367 (η_{1000})	46	1.58 (at 100 mA cm^{-2})	100 h (at 150 mA cm^{-2})	204
Ni–Fe–Mn–P/NC	Ni foam	1 M KOH	72 (η_{10})	80	274 (η_{30})	57	1.52	35 h (at 50 mA cm^{-2})	205
NaOH-ABC	Carbon cloth	0.5 M H_2SO_4	231 (η_{10})	168	155 (η_{10})	144	—	—	206
KOH-I ABC	Carbon cloth	0.5 M H_2SO_4	213 (η_{10})	146	126 (η_{10})	137	—	—	206
KOH-II ABC	Carbon cloth	0.5 M H_2SO_4	188 (η_{10})	137	90 (η_{10})	127	1.49	—	206
$NiCo_2O_4$-B-CC	Carbon cloth	Carbon cloth	26 (η_{10})	106	215 (η_{10})	95	400 (at 400 mA cm^{-2})	20 h (at 10 mA cm^{-2})	207

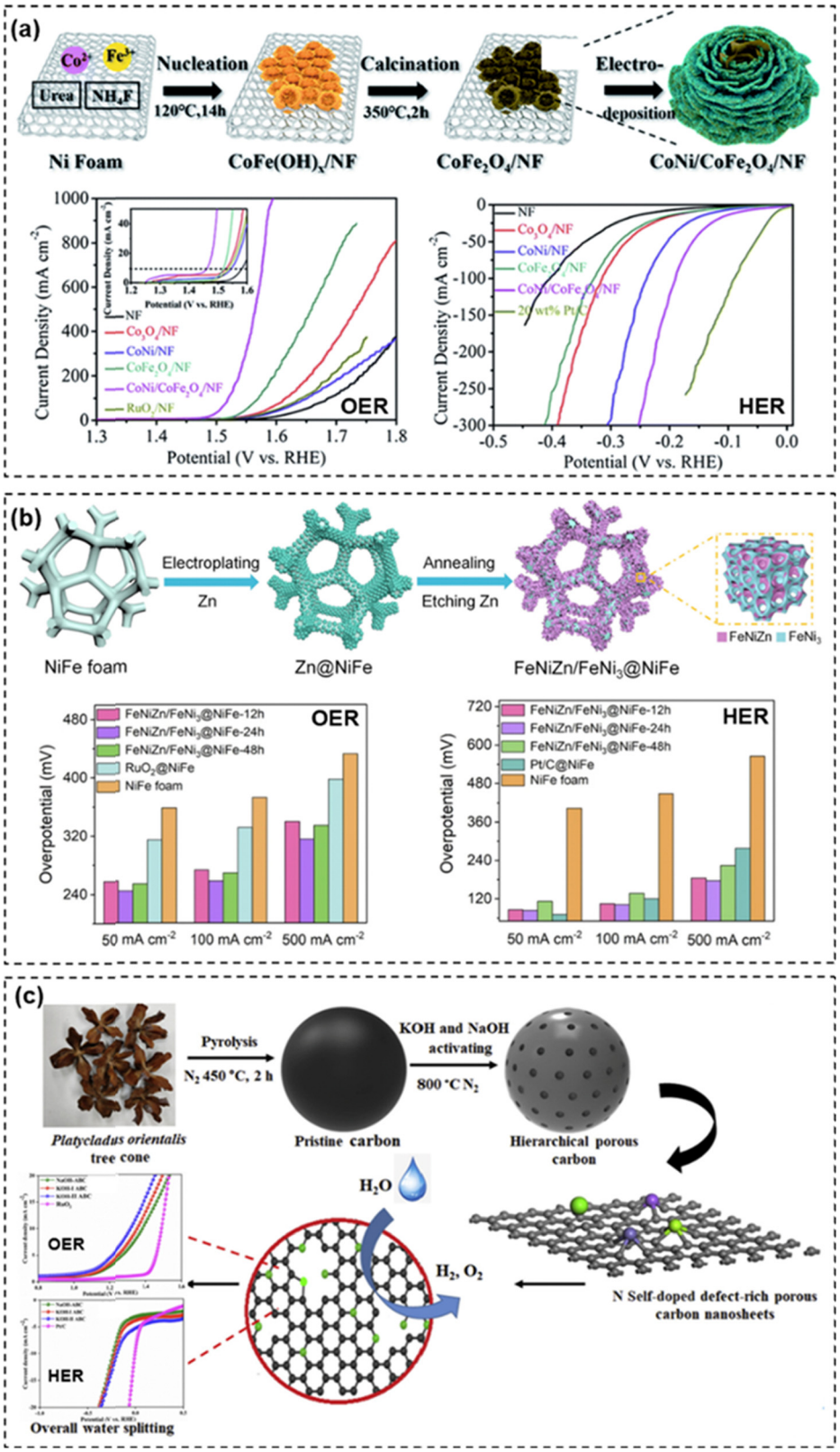

Fig. 14 **HER-OER** bifunctional electrocatalysts: Schematics of the preparation of (a) porous CoNi/$CoFe_2O_4$/NF and LSV curves,[189] (b) FeNiZn/$FeNi_3$@NiFe and comparison of the overpotentials[204] and (c) N-self-doped defect-rich porous carbon nanosheets and LSV curves.[206] Reproduced with permissions from ref. 189, Copyright 2018 Royal Society of Chemistry, ref. 204, Copyright 2023 Springer Nature, ref. 206 Copyright 2024 Elsevier.

overpotentials of 188 mV and 90 mV at 10 mA cm^{-2} in 0.5 M H_2SO_4 for **HER** and **OER**, respectively. In the overall water-splitting reaction using the metal-free nanosheet as both electrodes, a current density of 10 mA cm^{-2} was obtained at a low voltage of 1.49 V.

5.2. Seawater-splitting electrocatalysts

Currently, commercial water-splitting (*e.g.*, alkaline electrolysis cell and proton exchange membrane electrolysis cell) uses freshwater to produce hydrogen.[208] However, seawater is the most abundant resource, accounting for more than 97% of the water resources in the world.[209] However, the property of seawater (*e.g.*, high conductivity due to the presence of ionic species) is different from pure water and/or freshwater.[210] If water-splitting using seawater is carried out under the simulated conditions with a salt concentration of around 3.5%, seawater is electrolyzed without the addition of a conductive electrolyte (*e.g.*, KOH and H_2SO_4) and then hydrogen can possibly be produced with low cost.[211] A chlorine generation reaction with **OER** at the anode is another problem for seawater-splitting,[212,213] as well as the corrosion of the electrode at high Cl^- concentrations[214] and the deactivation of active sites by the coating of insoluble species.[215] To improve the activity, the selectivity and the durability of **OER** electrocatalysts under seawater conditions, including simulated seawater, and the overall efficiency of seawater-splitting at high current densities (>500 mA cm^{-2}), as listed in Table 7, has been investigated so far.

The design of a protective layer over an electrocatalyst is the most direct method to reduce the **OER** selectivity and Cl^- corrosion. The access of Cl^- to the active site is prevented by the presence of a protective layer. Feng *et al.* succeeded in fabricating an electrocatalyst (Ni_xFe_yN@C/NF) for seawater-splitting by growing an array of nickel–iron nitride microsheets coated with a carbon layer on Ni foam (see Fig. 15a).[223] In addition to the existence of many active sites, the mass and charge transport was accelerated by the superhydrophilic and superhydrophobic surfaces and the synergistic effect of the Ni_3FeN and carbon layers. Ni_xFe_yN@C/NF showed excellent **OER** overpotentials of 283 mV and 351 mV in alkaline simulated seawater at current densities of 100 mA cm^{-2} and 500 mA cm^{-2}, respectively, being very stable during the operation for up to 100 hours at a current density of 100 mA cm^{-2}. Surface poisoning by Cl^- as well as the surface deposition of insoluble species during seawater-splitting is prevented by enhancing hydrophilicity and wettability with surface modification of metal oxide derivative electrocatalysts.[233] Yang *et al.* succeeded in fabricating a hybrid electrocatalyst (Fe(Cr)OOH/Fe_3O_4/NF) with the hetero-interface of Fe(Cr)OOH and Fe_3O_4 on Ni foam (see Fig. 15b).[218] The super hydrophilic surface and high permeability of the electrolyte based on the introduced Cr (a first-row transition element with strong oxidizing properties) promoted electron transfer in the **OER** process, resulting in a small **OER** overpotential of 278 mV at a high current density of 500 mA cm^{-2} in simulated seawater. The electrolyzer using Fe(Cr)OOH/Fe_3O_4/NF as the anode achieved a current density of 10 mA cm^{-2} with a small cell voltage of 1.49 V and maintained a high current density of 400 mA cm^{-2} for 100 hours.

HER-OER bifunctional electrocatalysts are also very important in reducing the cost of green hydrogen production of seawater-splitting. The catalytic activity of porous nanostructured electrocatalysts can be adjusted in specific conditions by varying the electronic and surface environments. Several electrocatalysts have been developed so far to promote water electrolysis more efficiently on a lab scale than the typical benchmark IrO_2–Pt catalyst. There are several challenges to be dealt with to advance bifunctional electrocatalysts further for seawater-splitting. Theoretical predictions and *in situ* spectroscopic studies help in the detailed understanding of the reaction mechanisms and real-time structural changes of electrocatalysts during electrolysis. DFT calculation is also very useful for identifying the active species and optimizing electrocatalysts at the molecular level.[234] For the industrial use of seawater-splitting, in addition to designing electrocatalysts with high activity (η_{10} < 300 mV) and stability (operating for >1000 hours under high-density current of >500 mA cm^{-2}), a simple and low-cost pre-treatment process of natural seawater is necessary to alleviate corrosion

Table 7 **OER** performance of the reported porous **OER** catalysts in seawater-splitting

OER electrocatalyst	Substrate	Electrolyte	η (mV)	Tafel slope (mV dec^{-1})	Long-term stability	Ref.
S–NCFO	Ni foam	0.5 M NaCl + 1 M KOH	290 (η_{50})	32	48 h (at 100 mA cm^{-2})	216
Ni_xCr_yO	Carbon paper	Seawater + 1 M KOH	270 (η_{100})	—	280 h (at 500 mA cm^{-2})	217
Fe(Cr)OOH/Fe_3O_4	Ni foam	Seawater + 1 M KOH	278 (η_{500})	34	100 h (at 400 mA cm^{-2})	218
S–(Ni,Fe)OOH	Ni foam	Seawater + 1 M KOH	300 (η_{100})	49	100 h (at 100 mA cm^{-2})	219
CoFeZr	Ni foam	0.5 M NaCl + 1 M KOH	303 (η_{100})	41	20 h (at 100 mA cm^{-2})	220
NF/NiFe LDH	Ni foam	Seawater + 1 M KOH	247 (η_{100})	33	96 h (at 500 mA cm^{-2})	221
NiFe-LDH	Ni foam	0.5 M NaCl + 1 M KOH	257 (η_{500})	—	24 h (at 500 mA cm^{-2})	222
Ni_xFe_yN@C	Ni foam	Seawater + 1 M KOH	283 (η_{100})	45	100 h (at 500 mA cm^{-2})	223
Ni_2P–Fe_2P	Ni foam	Seawater + 1 M KOH	305 (η_{100})	58	38 h (at 500 mA cm^{-2})	224
S–NiFe–Pi	NiFe foam	Seawater + 1 M KOH	241 (η_{100})	52	100 h (at 500 mA cm^{-2})	225
ZnFe-BDC-0.75	Ni foam	Seawater	308 (η_{100})	48	50 h (at 10 mA cm^{-2})	226
Ni_3Fe-BDC	Flake graphite	1 M NaCl + 1 M KOH	295 (η_{10})	95	25 h (at 10 mA cm^{-2})	227
NH_2–NiCoFe–MIL-101	Ni foam	Seawater + 1 M KOH	390 (η_{1000})	48	90 h (at 60 mA cm^{-2})	228
MIL-88(FeCoNi) (HMIL-88@PPy-TA)	Ni foam	0.5 M NaCl + 1 M KOH	244 (η_{100})	46	100 h (at 100 mA cm^{-2})	229
NiFe-LDH/MOF	Ni foam	Seawater + 1 M KOH	235 (η_{20})	61	100 h (at 20 mA cm^{-2})	230
NiFe-MOF@Ni_2P/Ni$(OH)_2$	Ni foam	0.5 M NaCl + 1 M KOH	302 (η_{100})	43	120 h (at 500 mA cm^{-2})	231
Ni MOFs/FeS	Fe foam	Seawater + 1 M KOH	280 (η_{100})	55	25 h (at 100 mA cm^{-2})	232

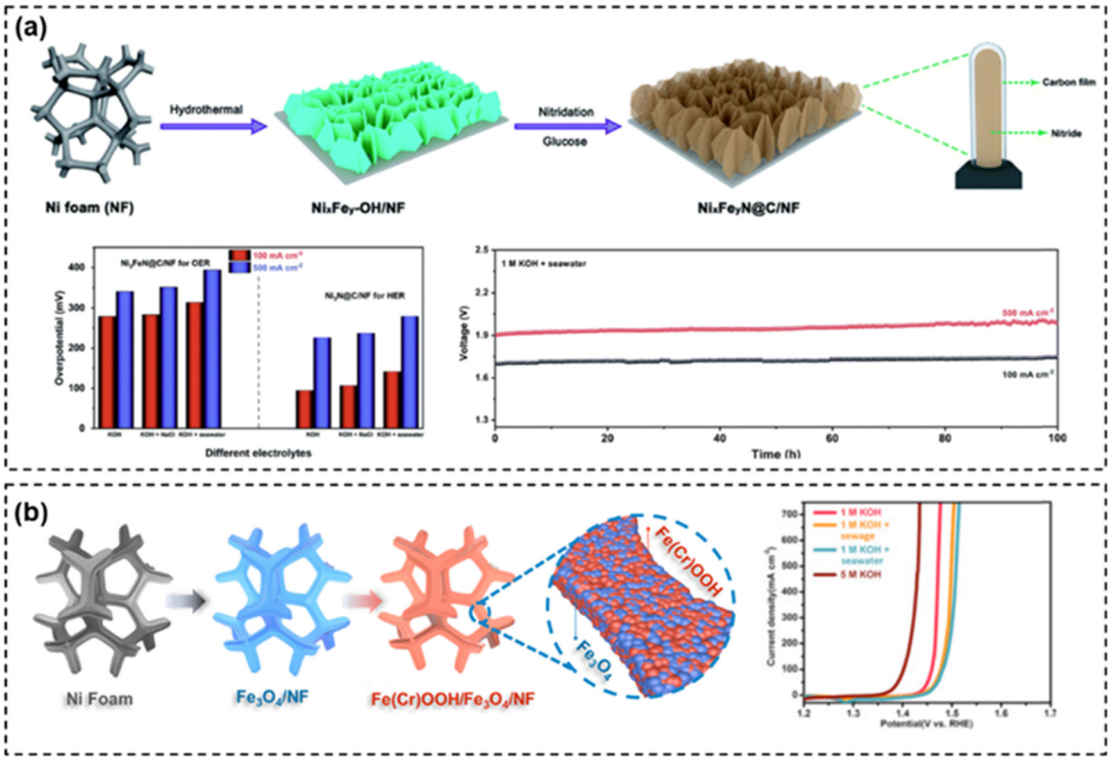

Fig. 15 Seawater-splitting **OER** electrocatalysts: Schematic of the preparation of (a) Ni_xFe_yN@C/NF with a comparison of the overpotentials for **HER** and **OER** at 100 mA cm^{-2} and 500 mA cm^{-2} in different electrolytes and durability tests of the electrolyzer at 100 mA cm^{-2} and 500 mA cm^{-2} in 1 M KOH and alkaline seawater in 1 M KOH[223] and (b) Fe(Cr)OOH/Fe_3O_4/NF with LSV curves for **OER** at high current densities measured in different electrolytes.[218] Reproduced with permissions from ref. 223, Copyright 2021 Royal Society of Chemistry, ref. 218, Copyright 2022 Elsevier.

and poisoning as much as possible, as well as smooth and selective **OER** even by using natural seawater.

6. Conclusions

The recent advances in the development of high-performance porous electrocatalysts were surveyed for achieving efficient water-splitting reactions (Fig. 1). This feature article mainly focused on the replacement of expensive and rare precious metal derivative electrocatalysts with inexpensive and comparable base metal electrocatalysts for cost-effective green hydrogen. For suggesting the detailed structural model for improving the catalytic activity, the resultant **OER** activity was reviewed by using structural features such as porosity (*e.g.*, specific surface area and pore volume) and surface structure (*e.g.*, accessible active hydroxyl groups) of inorganic-based materials (*e.g.*, oxides, hydroxides and phosphates of base metals) in addition to those (*e.g.*, highly dispersed metal clusters and designable organic linkers) of organic-based porous materials combined with surface functions and physical properties designed by using organic linkers. All-organic porous electrocatalysts have been designed by introducing electron-donating substituents and conductive frameworks, which improve the electronic conductivity and proton conductivity of organic frameworks and enhance **OER** activity. Unique open pores in the highly porous structure also facilitate the diffusion of reactants and products, promoting **OER**. Larger pores such as mesopores are also useful for an effective diffusion of reactants and products, which are, for example, tuned by the soft-templating with the self-assembly of amphiphilic organic molecules.[235,236] During the removal of the supramolecular organic templates, the structural variation of inorganic-based frameworks has been clarified with isotropic/anisotropic shrinkage of the mesoporous structures.[237,238] Molecularly arranged hybrid frameworks can also be designed for the mesostructural design of earth-abundant base metal phosphates containing organic functions.[239,240]

Exceptional qualities of small-sized transition metal oxide clusters are promising for utilizing metal cation defects and oxygen vacancies due to the presence of low-coordinated active sites, high-surface-energy amorphous structures, and so on.[241] Fundamentals on the mechanism (*e.g.*, lattice-oxygen oxidation mechanism and adsorbate evolution mechanism) and kinetics of **OER** have been disclosed further for the precise design of efficient electrocatalysts.[242] Further optimization of **OER** activity has also been investigated by using the synergistic catalytic effect, combining the property arising from the presence of multiple metals in the crystal structure of spinel oxides and LDHs, and adjusting the electronic environment of the metals by doping heteroatoms such as nitrogen and sulfur. In recent years, there have been many reports of base metal derivative electrocatalysts with **OER** activity comparable to those observed for conventional precious metal electrocatalysts such as IrO_2 and RuO_2.

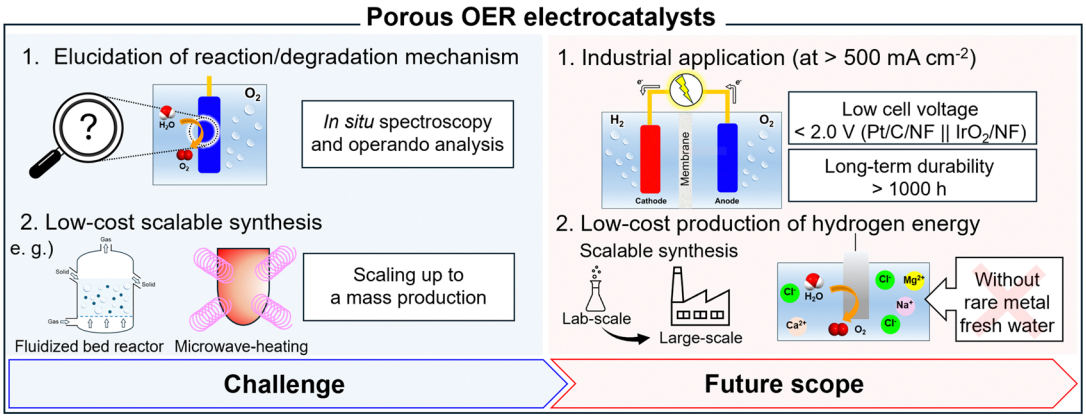

Fig. 16 Outline of the challenges and future scopes in porous **OER** electrocatalysts.

7. Challenges and future scope

Several concerns should be solved as future challenges to incorporate porous **OER** electrocatalysts into the existing water-splitting systems for producing low-cost and enough green hydrogen as the next-generation energy source (Fig. 16). After further elucidating the structure of the active site and the **OER** mechanism, the long-time durability of electrocatalysts should be improved at very high current densities (>500 mA cm^{-2}) during practical use. *In situ* spectroscopy and *operando* analysis are also effective for elucidating the state of electrocatalysts as well as for understanding the intermediate during **OER** reactions and the degradation mechanism of electrocatalysts. In particular, **OER** electrocatalysts in existing water-splitting systems must operate stably for at least 1000 hours under a current density of >500 mA cm^{-2}. Most porous **OER** electrocatalysts have not reached this standard. A low-cost scalable synthesis of porous **OER** electrocatalysts is also essential for practical use. For scaling up the mass production of the electrocatalysts, the quality as well as the catalytic performance must be maintained as much as possible. Base metal-based porous **OER** catalysts will be required for cost-effective hydrogen production.[243] Developing water-splitting technology, especially for eco-friendly seawater electrolysis, but not limited to freshwater, needs the precise design of electrocatalysts that can work effectively even in the presence of ionic species (*e.g.*, Na^+, Mg^{2+}, and Cl^-).[244] In addition to the rational design of such electrocatalysts, the environment of inner and outer electrodes would be quite important for proceeding with the reactions selectively to handle water molecules only at the surface of the electrodes.

Data availability

No primary research results, software or code have been included and no new data were generated or analyzed as part of this feature article.

Conflicts of interest

The author declares no competing financial interest.

Acknowledgements

This work was partly supported by the Japan Society for the Promotion of Science (JSPS) KAKENHI Grant Number JP23K17945, JP23H03827, JP24K01552, and 24KJ1580 and the Environment Research and Technology Development Fund (JPMEERF20241RA4) of the Environmental Restoration and Conservation Agency provided by the Ministry of the Environment of Japan. K. O. acknowledged the support from Shorai Foundation for Science and Technology, TEPCO Memorial Foundation, Amano Industry Technology Laboratory, Sugiyama Houkoukai, The Yamada Science Foundation, Kenjiro Takayanagi Foundation, Kansai Research Foundation for Technology Promotion, Yashima Environment Technology Foundation, JACI Prize for Encouraging Young Researcher, Foundation for Interaction in Science and Technology, Iketani Science and Technology Foundation, and Ichimura Foundation for New technology.

References

1 M. Chatenet, B. G. Pollet, D. R. Dekel, F. Dionigi, J. Deseure, P. Millet, R. D. Braatz, M. Z. Bazant, M. Eikerling and I. Staffell, *Chem. Soc. Rev.*, 2022, **51**, 4583–4762.
2 J. A. Turner, *Science*, 2004, **305**, 972–974.
3 X.-Y. Zhang, J.-Y. Xie, Y. Ma, B. Dong, C.-G. Liu and Y.-M. Chai, *J. Chem. Eng.*, 2022, **430**, 132312.
4 M. Chen, N. Kitiphatpiboon, C. Feng, A. Abudula, Y. Ma and G. Guan, *eScience*, 2023, **3**, 100111.
5 C.-J. Huang, H.-M. Xu, T.-Y. Shuai, Q.-N. Zhan, Z.-J. Zhang and G.-R. Li, *Appl. Catal., B*, 2023, **325**, 122313.
6 M. Yu, E. Budiyanto and H. Tüysüz, *Angew. Chem., Int. Ed.*, 2022, **61**, e202103824.
7 L. Giordano, B. Han, M. Risch, W. T. Hong, R. R. Rao, K. A. Stoerzinger and Y. Shao-Horn, *Catal. Today*, 2016, **262**, 2–10.
8 F. Schenke, J. Hoelzen, C. Minke, A. Bensmann and R. Hanke-Rauschenbach, *Energy Convers. Manage.*, 2023, **20**, 100435.
9 R. Riedmayer, B. A. Paren, L. Schofield, Y. Shao-Horn and D. Mallapragada, *Energy Fuels*, 2023, **37**, 8614–8623.
10 N. Pandey, S. K. Tripathy, S. K. Patra and G. Jha, *Trans. Indian Inst. Met.*, 2023, **76**, 11–30.
11 E. Savinova, C. Evans, É. Lèbre, M. Stringer, M. Azadi and R. K. Valenta, *Resour., Conserv. Recycl.*, 2023, **190**, 106855.
12 L. Han, S. Dong and E. Wang, *Adv. Mater.*, 2016, **28**, 9266–9291.
13 T. Guo, L. Li and Z. Wang, *Adv. Energy Mater.*, 2022, **12**, 2200827.
14 K. Zhang and R. Zou, *Small*, 2021, **17**, 2100129.
15 Y. Aykut and A. B. Yurtcan, *Electrochim. Acta*, 2023, **471**, 143335.

16 X. Li, X. Hao, A. Abudula and G. Guan, *J. Mater. Chem. A*, 2016, **4**, 11973–12000.
17 X. Qin, D. Kim and Y. Piao, *Carbon Energy*, 2021, **3**, 66–100.
18 L. Zu, W. Zhang, L. Qu, L. Liu, W. Li, A. Yu and D. Zhao, *Adv. Energy Mater.*, 2020, **10**, 2002152.
19 Y. Kang, Y. Guo, J. Zhao, B. Jiang, J. Guo, Y. Tang, H. Li, V. Malgras, M. A. Amin and H. Nara, *Small*, 2022, **18**, 2203411.
20 J. Qi, W. Zhang and R. Cao, *ChemCatChem*, 2018, **10**, 1206–1220.
21 X. Zhao, P. Pachfule and A. Thomas, *Chem. Soc. Rev.*, 2021, **50**, 6871–6913.
22 W. Lu, Z. Wei, Z.-Y. Gu, T.-F. Liu, J. Park, J. Park, J. Tian, M. Zhang, Q. Zhang and T. Gentle III, *Chem. Soc. Rev.*, 2014, **43**, 5561–5593.
23 D. Yu, H. Zhang, J. Ren and X. Qu, *Chem. Soc. Rev.*, 2023, **52**, 7504–7523.
24 J. Meng, X. Liu, C. Niu, Q. Pang, J. Li, F. Liu, Z. Liu and L. Mai, *Chem. Soc. Rev.*, 2020, **49**, 3142–3186.
25 H. Sei, K. Oka, T. Furuta and N. Tohnai, *Bull. Chem. Soc. Jpn.*, 2024, **97**, uoad023.
26 H. Sei, K. Oka and N. Tohnai, *ChemNanoMat*, 2023, **9**, e202300248.
27 H. Sei, K. Oka, H. Sotome, H. Miyasaka and N. Tohnai, *Small*, 2023, **19**, 2301887.
28 G. Hatakeyama, H. Zhou, T. Kikuchi, M. Nishio, K. Oka, M. Sadakiyo, Y. Nishiyama and T. Yamada, *Chem. Sci.*, 2023, **14**, 9068–9073.
29 T. Ami, K. Oka, K. Tsuchiya and N. Tohnai, *Angew. Chem., Int. Ed.*, 2022, **61**, e202202597.
30 T. Ami, K. Oka, K. Tsuchiya, W. Kosaka, H. Miyasaka and N. Tohnai, *CrystEngComm*, 2023, **25**, 2321–2325.
31 T. Ami, S. Kitajima, K. Oka and N. Tohnai, *Angew. Chem., Int. Ed.*, 2024, e202407484, DOI: **10.1002/anie.202407484**.
32 A. J. Bard, L. R. Faulkner and H. S. White, *Electrochemical methods: fundamentals and applications*, John Wiley & Sons, 2022.
33 M.-I. Jamesh and X. Sun, *J. Power Sources*, 2018, **400**, 31–68.
34 T. Reier, H. N. Nong, D. Teschner, R. Schlögl and P. Strasser, *Adv. Energy Mater.*, 2017, **7**, 1601275.
35 K. Oka, B. Winther-Jensen and H. Nishide, *Adv. Energy Mater.*, 2021, **11**, 2003724.
36 W. T. Hong, M. Risch, K. A. Stoerzinger, A. Grimaud, J. Suntivich and Y. Shao-Horn, *Energy Environ. Sci.*, 2015, **8**, 1404–1427.
37 H. Xu, H. Shang, C. Wang and Y. Du, *Coord. Chem. Rev.*, 2020, **418**, 213374.
38 H. Sun, X. Xu, H. Kim, W. Jung, W. Zhou and Z. Shao, *Energy Environ. Mater.*, 2023, **6**, e12441.
39 Z. Lei, T. Wang, B. Zhao, W. Cai, Y. Liu, S. Jiao, Q. Li, R. Cao and M. Liu, *Adv. Energy Mater.*, 2020, **10**, 2000478.
40 J. T. Mefford, X. Rong, A. M. Abakumov, W. G. Hardin, S. Dai, A. M. Kolpak, K. P. Johnston and K. J. Stevenson, *Nat. Commun.*, 2016, **7**, 11053.
41 I. C. Man, H. Y. Su, F. Calle-Vallejo, H. A. Hansen, J. I. Martínez, N. G. Inoglu, J. Kitchin, T. F. Jaramillo, J. K. Nørskov and J. Rossmeisl, *ChemCatChem*, 2011, **3**, 1159–1165.
42 J. Ying, J.-B. Chen, Y.-X. Xiao, S. I. Cordoba de Torresi, K. I. Ozoemena and X.-Y. Yang, *J. Mater. Chem. A*, 2023, **11**, 1634–1650.
43 Y. Zhang, Q. Fu, B. Song and P. Xu, *Acc. Mater. Res.*, 2022, **3**, 1088–1100.
44 L. Xu, Q. Jiang, Z. Xiao, X. Li, J. Huo, S. Wang and L. Dai, *Angew. Chem., Int. Ed.*, 2016, **128**, 5363–5367.
45 S. Wan, J. Qi, W. Zhang, W. Wang, S. Zhang, K. Liu, H. Zheng, J. Sun, S. Wang and R. Cao, *Adv. Mater.*, 2017, **29**, 1700286.
46 G. T. Burstein, *Corros. Sci.*, 2005, **47**, 2858–2870.
47 T. Grewe, X. Deng, C. Weidenthaler, F. Schüth and H. Tüysüz, *Chem. Mater.*, 2013, **25**, 4926–4935.
48 J. Qi, W. Zhang, R. Xiang, K. Liu, H.-Y. Wang, M. Chen, Y. Han and R. Cao, *Adv. Sci.*, 2015, **2**, 1500199.
49 M.-S. Balogun, W. Qiu, H. Yang, W. Fan, Y. Huang, P. Fang, G. Li, H. Ji and Y. Tong, *Energy Environ. Sci.*, 2016, **9**, 3411–3416.
50 Y. Wu, M. Chen, Y. Han, H. Luo, X. Su, M.-T. Zhang, X. Lin, J. Sun, L. Wang, L. Deng, W. Zhang and R. Cao, *Angew. Chem., Int. Ed.*, 2015, **54**, 4870–4875.
51 F. Yu, H. Zhou, Z. Zhu, J. Sun, R. He, J. Bao, S. Chen and Z. Ren, *ACS Catal.*, 2017, **7**, 2052–2057.
52 S. Kitagawa, *Chem. Soc. Rev.*, 2014, **43**, 5415–5418.
53 H. Furukawa, K. E. Cordova, M. O'Keeffe and O. M. Yaghi, *Science*, 2013, **341**, 1230444.
54 S. L. James, *Chem. Soc. Rev.*, 2003, **32**, 276–288.
55 O. M. Yaghi, G. Li and H. Li, *Nature*, 1995, **378**, 703–706.
56 H. Mistry, Y. W. Choi, A. Bagger, F. Scholten, C. S. Bonifacio, I. Sinev, N. J. Divins, I. Zegkinoglou, H. S. Jeon and K. Kisslinger, *Angew. Chem., Int. Ed.*, 2017, **129**, 11552–11556.
57 S. Piracha, Y. Zhang, A. Raza and G. Li, *Chem. Commun.*, 2024, **60**, 9918–9929.
58 X. Deng and H. Tüysüz, *ACS Catal.*, 2014, **4**, 3701–3714.
59 R. Poulain, A. Klein and J. Proost, *J. Phys. Chem. C*, 2018, **122**, 22252–22263.
60 A. Bergmann, E. Martinez-Moreno, D. Teschner, P. Chernev, M. Gliech, J. F. de Araújo, T. Reier, H. Dau and P. Strasser, *Nat. Commun.*, 2015, **6**, 8625.
61 S. Liu, I. Zaharieva, L. D'Amario, S. Mebs, P. Kubella, F. Yang, P. Beyer, M. Haumann and H. Dau, *Adv. Energy Mater.*, 2022, **12**, 2202914.
62 R. A. E. Acedera, G. Gupta, M. Mamlouk and M. D. L. Balela, *J. Alloys Compd.*, 2020, **836**, 154919.
63 Z. Li, X.-Y. Yu and U. Paik, *J. Power Sources*, 2016, **310**, 41–46.
64 D. Tang, Y. Ma, Y. Liu, K. Wang, Z. Liu, W. Li and J. Li, *J. Alloys Compd.*, 2022, **893**, 162287.
65 S. Gupta, A. Yadav, S. Bhartiya, M. K. Singh, A. Miotello, A. Sarkar and N. Patel, *Nanoscale*, 2018, **10**, 8806–8819.
66 P. Yan, M. Huang, B. Wang, Z. Wan, M. Qian, H. Yan, T. T. Isimjan, J. Tian and X. Yang, *J. Energy Chem.*, 2020, **47**, 299–306.
67 H. Zhang, S. Geng, M. Ouyang, M. Mao, F. Xie and D. J. Riley, *Small*, 2022, **18**, 2106391.
68 W. Xu, F. Lyu, Y. Bai, A. Gao, J. Feng, Z. Cai and Y. Yin, *Nano Energy*, 2018, **43**, 110–116.
69 H. Xia, Z. Huang, C. Lv and C. Zhang, *ACS Catal.*, 2017, **7**, 8205–8213.
70 P. Babar, A. Lokhande, M. Gang, B. Pawar, S. Pawar and J. H. Kim, *J. Ind. Eng. Chem.*, 2018, **60**, 493–497.
71 J. Qi, W. Zhang, R. Xiang, K. Liu, H.-Y. Wang, M. Chen, Y. Han and R. Cao, *Adv. Sci.*, 2015, **2**, 1500199.
72 T. Tian, H. Gao, X. Zhou, L. Zheng, J. Wu, K. Li and Y. Ding, *ACS Energy Lett.*, 2018, **3**, 2150–2158.
73 Y. Shen, S.-G. Guo, F. Du, X.-B. Yuan, Y. Zhang, J. Hu, Q. Shen, W. Luo, A. Alsaedi and T. Hayat, *Nanoscale*, 2019, **11**, 11765–11773.
74 Y. Li, P. Hasin and Y. Wu, *Adv. Mater.*, 2010, **17**, 1926–1929.
75 L. Kuai, J. Geng, C. Chen, E. Kan, Y. Liu, Q. Wang and B. Geng, *Angew. Chem., Int. Ed.*, 2014, **53**, 7547–7551.
76 Y. Gong, H. Pan, Z. Xu, Z. Yang, Y. Lin and M. Zhang, *Int. J. Hydrogen Energy*, 2018, **43**, 14360–14368.
77 L. He, H. Kang, G. Hou, X. Qiao, X. Jia, W. Qin and X. Wu, *J. Chem. Eng.*, 2023, **460**, 141675.
78 Y. Li, F.-M. Li, X.-Y. Meng, X.-R. Wu, S.-N. Li and Y. Chen, *Nano Energy*, 2018, **54**, 238–250.
79 T. Grewe, X. Deng and H. Tüysüz, *Chem. Mater.*, 2014, **26**, 3162–3168.
80 J. Zhao, X.-R. Wang, X.-J. Wang, Y.-P. Li, X.-D. Yang, G.-D. Li and F.-T. Li, *Inorg. Chem. Front.*, 2018, **5**, 1886–1893.
81 H. Shi and G. Zhao, *J. Phys. Chem. C*, 2014, **118**, 25939–25946.
82 J. Yin, P. Zhou, L. An, L. Huang, C. Shao, J. Wang, H. Liu and P. Xi, *Nanoscale*, 2016, **8**, 1390–1400.
83 L. Tao, Y. Li, M. Li, G. Gao, X. Xiao, M. Wang, X. Jiang, X. Lv, Q. Li and S. Zhang, *J. Phys. Chem. C*, 2017, **121**, 25888–25897.
84 Y. Huang, W. Yang, Y. Yu and S. Hao, *J. Electroanal. Chem.*, 2019, **840**, 409–414.
85 M. Li, Y. Xiong, X. Liu, X. Bo, Y. Zhang, C. Han and L. Guo, *Nanoscale*, 2015, **7**, 8920–8930.
86 X. Liu, Z. Chang, L. Luo, T. Xu, X. Lei, J. Liu and X. Sun, *Chem. Mater.*, 2014, **26**, 1889–1895.
87 J. Zhang, D. Zhang, Y. Yang, J. Ma, S. Cui, Y. Li and B. Yuan, *RSC Adv.*, 2016, **6**, 92699–92704.
88 M. S. Amer, P. Arunachalam, M. A. Ghanem, A. M. Al-Mayouf and M. A. Shar, *Appl. Surf. Sci.*, 2020, **513**, 145831.
89 W. Yaseen, N. Ullah, M. Xie, B. A. Yusuf, Y. Xu, C. Tong and J. Xie, *Surf. Interfaces*, 2021, **26**, 101361.
90 Y. Sun, S. Gao, F. Lei, J. Liu, L. Liang and Y. Xie, *Chem. Sci.*, 2014, **5**, 3976–3982.
91 Q. Qu, J.-H. Zhang, J. Wang, Q.-Y. Li, C.-W. Xu and X. Lu, *Sci. Rep.*, 2017, **7**, 41542.
92 Q. Zhao, Z. Yan, C. Chen and J. Chen, *Chem. Rev.*, 2017, **117**, 10121–10211.

93 X. Wang, Z. Wang, Y. Cao, X. Liu, L. Zhou, J. Shi, B. Guo, D. Li, R. Ye and Z. Zhao, *J. Solid State Chem.*, 2024, **331**, 124553.
94 S. Nishikawa, *Proc. Tokyo Math.-Phys. Soc.*, 1915, **8**, 199–209.
95 W. Bragg, *Nature*, 1915, **95**, 561.
96 F. Cheng, J. Shen, B. Peng, Y. Pan, Z. Tao and J. Chen, *Nat. Chem.*, 2011, **3**, 79–84.
97 O. Y. M. N. Avcı, L. Sementa and A. Fortunelli, *ACS Catal.*, 2022, **12**, 9058–9073.
98 E. M. Davis, A. Bergmann, C. Zhan, H. Kuhlenbeck and B. R. Cuenya, *Nat. Commun.*, 2023, **14**, 4791.
99 Z. Cai, X. Bu, P. Wang, J. C. Ho, J. Yang and X. Wang, *J. Mater. Chem. A*, 2019, **7**, 5069–5089.
100 F. Song, L. Bai, A. Moysiadou, S. Lee, C. Hu, L. Liardet and X. Hu, *J. Am. Chem. Soc.*, 2018, **140**, 7748–7759.
101 C. Tang, H. F. Wang, X. L. Zhu, B. Q. Li and Q. Zhang, *Part. Part. Syst. Charact.*, 2016, **33**, 473–486.
102 C. Li, M. Wei, D. G. Evans and X. Duan, *Small*, 2014, **10**, 4469–4486.
103 J. B. Gerken, S. E. Shaner, R. C. Massé, N. J. Porubsky and S. S. Stahl, *Energy Environ. Sci.*, 2014, **7**, 2376–2382.
104 D. Hall, *J. Electrochem. Soc.*, 1983, **130**, 317.
105 M. Bukhtiyarova, *J. Solid State Chem.*, 2019, **269**, 494–506.
106 M. A. Ghanem, A. M. Al-Mayouf, P. Arunachalam and T. Abiti, *Electrochim. Acta*, 2016, **207**, 177–186.
107 C. Jing, T. Yuan, L. Li, J. Li, Z. Qian, J. Zhou, Y. Wang, S. Xi, N. Zhang and H.-J. Lin, *ACS Catal.*, 2022, **12**, 10276–10284.
108 C. G. Morales-Guio, L. Liardet and X. Hu, *J. Am. Chem. Soc.*, 2016, **138**, 8946–8957.
109 Z. Lu, W. Xu, W. Zhu, Q. Yang, X. Lei, J. Liu, Y. Li, X. Sun and X. Duan, *Chem. Commun.*, 2014, **50**, 6479–6482.
110 J. Zhang, C. Dong, Z. Wang, C. Zhang, H. Gao, J. Niu and Z. Zhang, *Electrochim. Acta*, 2018, **284**, 495–503.
111 T. Kou, S. Wang, J. L. Hauser, M. Chen, S. R. Oliver, Y. Ye, J. Guo and Y. Li, *ACS Energy Lett.*, 2019, **4**, 622–628.
112 P. Guo, J. Wu, X.-B. Li, J. Luo, W.-M. Lau, H. Liu, X.-L. Sun and L.-M. Liu, *Nano Energy*, 2018, **47**, 96–104.
113 W. Liang, M. Wang, C. Ma, J. Wang, C. Zhao and C. Hong, *Small*, 2024, **20**, 2306473.
114 P. Aggarwal, P. Mehra and A. Paul, *ACS Appl. Nano Mater.*, 2024, **7**, 9532–9541.
115 J. Long, J. Zhang, X. Xu and F. Wang, *Mater. Chem. Phys.*, 2020, **254**, 123496.
116 W. Zhu, T. Zhang, Y. Zhang, Z. Yue, Y. Li, R. Wang, Y. Ji, X. Sun and J. Wang, *Appl. Catal., B*, 2019, **244**, 844–852.
117 J. Jiang, A. Zhang, L. Li and L. Ai, *J. Power Sources*, 2015, **278**, 445–451.
118 L. Feng, Y. Du, J. Huang, L. Cao, L. Feng, Y. Feng, Q. Liu, D. Yang and K. Kajiyoshi, *Sustainable Energy Fuels*, 2020, **4**, 2850–2858.
119 H. Zhang, X. Li, A. Hähnel, V. Naumann, C. Lin, S. Azimi, S. L. Schweizer, A. W. Maijenburg and R. B. Wehrspohn, *Adv. Funct. Mater.*, 2018, **28**, 1706847.
120 H. Sun, J.-M. Yang, J.-G. Li, Z. Li, X. Ao, Y.-Z. Liu, Y. Zhang, Y. Li, C. Wang and J. Tang, *Appl. Catal., B*, 2020, **272**, 118988.
121 P. Li, X. Duan, Y. Kuang, Y. Li, G. Zhang, W. Liu and X. Sun, *Adv. Energy Mater.*, 2018, **8**, 1703341.
122 P. Babar, A. Lokhande, V. Karade, B. Pawar, M. G. Gang, S. Pawar and J. H. Kim, *ACS Sustainable Chem. Eng.*, 2019, **7**, 10035–10043.
123 S.-W. Wu, S.-Q. Liu, X.-H. Tan, W.-Y. Zhang, K. Cadien and Z. Li, *J. Chem. Eng.*, 2022, **442**, 136105.
124 S. Hussain, D. Vikraman, G. Nazir, M. T. Mehran, F. Shahzad, K. M. Batoo, H.-S. Kim and J. Jung, *Nanomaterials*, 2022, **12**, 2886.
125 K. Zhang, F. Wang, X. Li, S. Wang, Y. Wang, Q. Zha and Y. Ni, *J. Alloys Compd.*, 2023, **942**, 169014.
126 Z. Zhang, Z. Wang, H. Zhang, Z. Zhang, J. Zhou, Y. Hou, P. Liu, B. Xu, H. Zhang and J. Guo, *J. Mater. Chem.*, 2023, **11**, 4355–4364.
127 X. Deng, H. Qin, X. Liu, S. Zhu, J. Li, L. Ma and N. Zhao, *J. Alloys Compd.*, 2022, **918**, 165650.
128 Z. Li, W. J. Kang, H. Liu, X. W. Du, F. Wang, Y. Song, Y. Liu, D. L. Sun and F. Fang, *Adv. Funct. Mater.*, 2023, **33**, 2301947.
129 V. K. Magotra, A. Magotra, S. S. Mali, H. C. Jeon, T. W. Kang, A. S. Salunke, C. K. Hong, N. K. Shrestha, H. Im and A. I. Inamdar, *Membranes*, 2023, **13**, 748.
130 J. Ye, B. Yuan, W. Peng, J. Liang, Q. Han and R. Hu, *ACS Appl. Mater. Interfaces*, 2024, **16**, 23189–23198.
131 C. Pitchai, M. Vedanarayanan, C.-M. Chen and S. M. Gopalakrishnan, *Int. J. Hydrogen Energy*, 2024, **72**, 755–763.
132 X. Zhu, C. Tang, H.-F. Wang, B.-Q. Li, Q. Zhang, C. Li, C. Yang and F. Wei, *J. Mater. Chem. A*, 2016, **4**, 7245–7250.
133 A.-L. Wang, H. Xu and G.-R. Li, *ACS Energy Lett.*, 2016, **1**, 445–453.
134 H. Zhao and Z.-Y. Yuan, *Catal. Sci. Technol.*, 2017, **7**, 330–347.
135 C. Chen, W. Chen, J. Lu, D. Chu, Z. Huo, Q. Peng and Y. Li, *Angew. Chem., Int. Ed.*, 2009, **121**, 4910–4913.
136 R. Murugavel, A. Choudhury, M. G. Walawalkar, R. Pothiraja and C. N. R. Rao, *Chem. Rev.*, 2008, **108**, 3549–3655.
137 M. W. Kanan and D. G. Nocera, *Science*, 2008, **321**, 1072–1075.
138 H. Zhao and Z. Y. Yuan, *ChemCatChem*, 2020, **12**, 3797–3810.
139 H.-L. Huang, Y.-T. Huang and S.-L. Wang, *Inorg. Chem. Front.*, 2016, **55**, 6836–6838.
140 Y. Zhao, J. Ju, X. Chen, X. Li, Y. Wang, R. Wang, M. Li and Z. Mai, *J. Solid State Chem.*, 2002, **166**, 369–374.
141 S. H. Jhung, J.-S. Chang, S.-E. Park, P. M. Förster, G. Férey and A. K. Cheetham, *Chem. Mater.*, 2004, **16**, 1394–1396.
142 H. S. Sonwalkar and S. K. Haram, *ChemistrySelect*, 2017, **2**, 3323–3328.
143 M. Pramanik, C. Li, M. Imura, V. Malgras, Y.-M. Kang and Y. Yamauchi, *Small*, 2016, **12**, 1709–1715.
144 L. Xie, R. Zhang, L. Cui, D. Liu, S. Hao, Y. Ma, G. Du, A. M. Asiri and X. Sun, *Angew. Chem., Int. Ed.*, 2017, **56**, 1064–1068.
145 J. Li, W. Xu, D. Zhou, J. Luo, D. Zhang, P. Xu, L. Wei and D. Yuan, *J. Mater. Sci.*, 2018, **53**, 2077–2086.
146 L. Chen, J.-T. Ren, Y.-S. Wang, W.-W. Tian, L.-J. Gao and Z.-Y. Yuan, *ACS Sustainable Chem. Eng.*, 2019, **7**, 13559–13568.
147 J. Zhang, Y. Yang, Z. Zhang, X. Xu and X. Wang, *J. Mater. Chem. A*, 2014, **2**, 20182–20188.
148 J. Xu, D. Xiong, I. Amorim and L. Liu, *ACS Appl. Nano Mater.*, 2018, **1**, 617–624.
149 D. Kim, J. Kang, B. Yan, K.-D. Seong and Y. Piao, *ACS Sustainable Chem. Eng.*, 2020, **8**, 2843–2853.
150 L. Pradhan, R. I. Mohanty, R. Bal, S. Basu, B. K. Jena and P. Bhanja, *Catal. Today*, 2023, **424**, 113771.
151 W. Xu, L. Feng, Z. Wang, B. Liu, X. Li and Y. Chen, *J. Electroanal. Chem.*, 2020, **879**, 114786.
152 P. Bhanja, Y. Kim, K. Kani, B. Paul, T. Debnath, J. Lin, A. Bhaumik and Y. Yamauchi, *J. Chem. Eng.*, 2020, **396**, 125245.
153 Y. Zhou and H. C. Zeng, *Small*, 2018, **14**, 1704403.
154 T. Kimura, *Angew. Chem., Int. Ed.*, 2017, **56**, 13459–13463.
155 A. Takamori and T. Kimura, *Langmuir*, 2023, **39**, 10680–10691.
156 Z. Chen, Q. Fan, J. Zhou, X. Wang, M. Huang, H. Jiang and H. Cölfen, *Angew. Chem., Int. Ed.*, 2023, **62**, e202309293.
157 X. Wang, H. Xiao, A. Li, Z. Li, S. Liu, Q. Zhang, Y. Gong, L. Zheng, Y. Zhu, C. Chen, D. Wang, Q. Peng, L. Gu, X. Han, J. Li and Y. Li, *J. Am. Chem. Soc.*, 2018, **140**, 15336–15341.
158 Y. Li, Z. Gao, H. Bao, B. Zhang, C. Wu, C. Huang, Z. Zhang, Y. Xie and H. Wang, *J. Energy Chem.*, 2021, **53**, 251–259.
159 S. Öztürk, G.-h Moon, A. Spieß, E. Budiyanto, S. Roitsch, H. Tüysüz and C. Janiak, *ChemPlusChem*, 2021, **86**, 1106–1115.
160 Y. Wang, B. Liu, X. Shen, H. Arandiyan, T. Zhao, Y. Li, M. Garbrecht, Z. Su, L. Han, A. Tricoli and C. Zhao, *Adv. Energy Mater.*, 2021, **11**, 2003759.
161 F. Zheng, D. Xiang, P. Li, Z. Zhang, C. Du, Z. Zhuang, X. Li and W. Chen, *ACS Sustainable Chem. Eng.*, 2019, **7**, 9743–9749.
162 C. Chen, J. Wang, P. Li, Q. Tian, Z. Xiao, S. Li, N. Cai, Y. Xue, W. Chen and F. Yu, *ChemCatChem*, 2021, **13**, 346–352.
163 Z. Li, S. Deng, H. Yu, Z. Yin, S. Qi, L. Yang, J. Lv, Z. Sun and M. Zhang, *J. Mater. Chem. A*, 2022, **10**, 4230–4241.
164 S. Zhou, T. Liu, M. Strømme and C. Xu, *Angew. Chem., Int. Ed.*, 2024, **63**, e202318387.
165 J. Liu, S. Zhao, C. Wang, B. Hu, L. He, M. Wang, Z. Zhang and M. Du, *Adv. Mater. Interfaces*, 2022, **9**, 2200913.
166 H. Jia, Y. Yao, J. Zhao, Y. Gao, Z. Luo and P. Du, *J. Mater. Chem. A*, 2018, **6**, 1188–1195.
167 W.-H. Li, J. Lv, Q. Li, J. Xie, N. Ogiwara, Y. Huang, H. Jiang, H. Kitagawa, G. Xu and Y. Wang, *J. Mater. Chem. A*, 2019, **7**, 10431–10438.
168 C. Jiao, M. Hu, T. Hu and J. Zhang, *J. Solid State Chem.*, 2023, **322**, 123978.
169 D. Xing, Y. Wang, P. Zhou, Y. Liu, Z. Wang, P. Wang, Z. Zheng, H. Cheng, Y. Dai and B. Huang, *Appl. Catal., B*, 2020, **278**, 119295.

170 Z. Lu, K. Wang, Y. Cao, Y. Li and D. Jia, *J. Alloys Compd.*, 2021, **871**, 159580.
171 B. Mishra, S. Biswal and B. P. Tripathi, *ACS Appl. Nano Mater.*, 2024, **7**, 5317–5328.
172 Q. Qi, Y. Zhang, C. Zhang, F. Liu, R. Liu and J. Hu, *J. Phys. Chem. C*, 2024, **128**, 1936–1945.
173 Z. Xue, Y. Li, Y. Zhang, W. Geng, B. Jia, J. Tang, S. Bao, H.-P. Wang, Y. Fan, Z.-W. Wei, Z. Zhang, Z. Ke, G. Li and C.-Y. Su, *Adv. Energy Mater.*, 2018, **8**, 1801564.
174 A. J. Clough, J. W. Yoo, M. H. Mecklenburg and S. C. Marinescu, *J. Am. Chem. Soc.*, 2015, **137**, 118–121.
175 E. M. Miner, T. Fukushima, D. Sheberla, L. Sun, Y. Surendranath and M. Dincă, *Nat. Commun.*, 2016, **7**, 10942.
176 R. Dong, Z. Zheng, D. C. Tranca, J. Zhang, N. Chandrasekhar, S. Liu, X. Zhuang, G. Seifert and X. Feng, *Chem. – Eur. J.*, 2017, **23**, 2255–2260.
177 X.-H. Liu, W.-L. Hu, W.-J. Jiang, Y.-W. Yang, S. Niu, B. Sun, J. Wu and J.-S. Hu, *ACS Appl. Mater. Interfaces*, 2017, **9**, 28473–28477.
178 M. Zhang, B.-H. Zheng, J. Xu, N. Pan, J. Yu, M. Chen and H. Cao, *Chem. Commun.*, 2018, **54**, 13579–13582.
179 M. Zhang, Q. Lin, W. Wu, Y. Ye, Z. Yao, X. Ma, S. Xiang and Z. Zhang, *ACS Appl. Mater. Interfaces*, 2020, **12**, 16367–16375.
180 B. Peng, D. Yang, Z. Li, H. Yuan, P. Wu, K. Huang, K. Sun, J. Zhu, K. Wu and Z. Liu, *J. Ind. Eng. Chem.*, 2024, **136**, 341–348.
181 C.-Y. Lin, D. Zhang, Z. Zhao and Z. Xia, *Adv. Mater.*, 2018, **30**, 1703646.
182 H. B. Aiyappa, J. Thote, D. B. Shinde, R. Banerjee and S. Kurungot, *Chem. Mater.*, 2016, **28**, 4375–4379.
183 H. Huang, F. Li, Y. Zhang and Y. Chen, *J. Mater. Chem. A*, 2019, **7**, 5575–5582.
184 Y. Zhao, Y. Yang, T. Xia, H. Tian, Y. Li, Z. Sui, N. Yuan, X. Tian and Q. Chen, *ChemSusChem*, 2021, **14**, 4556–4562.
185 Y. Liang, T. Xia, Z. Wu, Y. Yang, Y. Li, Z. Sui, C. Li, R. Fan, X. Tian and Q. Chen, *Mater. Today Chem.*, 2022, **24**, 100777.
186 M. Punniyamoorthy, S. Singha Roy, M. Kathiresan and S. Kundu, *ACS Appl. Energy Mater.*, 2024, **7**, 4111–4120.
187 S. Cobo, J. Heidkamp, P.-A. Jacques, J. Fize, V. Fourmond, L. Guetaz, B. Jousselme, V. Ivanova, H. Dau, S. Palacin, M. Fontecave and V. Artero, *Nat. Mater.*, 2012, **11**, 802–807.
188 T. R. Cook, D. K. Dogutan, S. Y. Reece, Y. Surendranath, T. S. Teets and D. G. Nocera, *Chem. Rev.*, 2010, **110**, 6474–6502.
189 S. Li, S. Sirisomboonchai, A. Yoshida, X. An, X. Hao, A. Abudula and G. Guan, *J. Mater. Chem. A*, 2018, **6**, 19221–19230.
190 F. Yu, H. Zhou, Y. Huang, J. Sun, F. Qin, J. Bao, W. A. Goddard, S. Chen and Z. Ren, *Nat. Commun.*, 2018, **9**, 2551.
191 Y. Yang, H. Fei, G. Ruan and J. M. Tour, *Adv. Mater.*, 2015, **27**, 3175–3180.
192 Y. Wang, D. Liu, Z. Liu, C. Xie, J. Huo and S. Wang, *Chem. Commun.*, 2016, **52**, 12614–12617.
193 S. Cui, M. Qian, X. Liu, Z. Sun and P. Du, *ChemSusChem*, 2016, **9**, 2365–2373.
194 G.-F. Chen, T. Y. Ma, Z.-Q. Liu, N. Li, Y.-Z. Su, K. Davey and S.-Z. Qiao, *Adv. Funct. Mater.*, 2016, **26**, 3314–3323.
195 Y. Jin, H. Wang, J. Li, X. Yue, Y. Han, P. K. Shen and Y. Cui, *Adv. Mater.*, 2016, **28**, 3785–3790.
196 B. You, N. Jiang, M. Sheng, M. W. Bhushan and Y. Sun, *ACS Catal.*, 2016, **6**, 714–721.
197 C. Xiao, Y. Li, X. Lu and C. Zhao, *Adv. Funct. Mater.*, 2016, **26**, 3515–3523.
198 X. Zou, Y. Wu, Y. Liu, D. Liu, W. Li, L. Gu, H. Liu, P. Wang, L. Sun and Y. Zhang, *Chem*, 2018, **4**, 1139–1152.
199 K. N. Dinh, P. Zheng, Z. Dai, Y. Zhang, R. Dangol, Y. Zheng, B. Li, Y. Zong and Q. Yan, *Small*, 2018, **14**, 1703257.
200 Z. Liu, X. Yu, H. Xue and L. Feng, *J. Mater. Chem. A*, 2019, **7**, 13242–13248.
201 Z. Cai, X. Bu, P. Wang, W. Su, R. Wei, J. C. Ho, J. Yang and X. Wang, *J. Mater. Chem. A*, 2019, **7**, 21722–21729.
202 P. W. Menezes, C. Panda, C. Walter, M. Schwarze and M. Driess, *Adv. Funct. Mater.*, 2019, **29**, 1808632.
203 A. Li, L. Zhang, F. Wang, L. Zhang, L. Li, H. Chen and Z. Wei, *Appl. Catal., B*, 2022, **310**, 121353.
204 Q. Zhou, C. Xu, J. Hou, W. Ma, T. Jian, S. Yan and H. Liu, *Nano-Micro Lett.*, 2023, **15**, 95.
205 R. B. Ghising, U. N. Pan, D. R. Paudel, M. R. Kandel, N. H. Kim and J. H. Lee, *J. Mater. Chem. A*, 2022, **10**, 16457–16467.
206 N. Murugan, S. Thangarasu, S. B. Seo, A. Mariappan, Y. R. Choi, T. H. Oh and Y. A. Kim, *Renewable Energy*, 2024, **222**, 119801.
207 M. Wang, X. Feng, S. Li, Y. Ma, Y. Peng, S. Yang, Y. Liu, H. Lei, J. Dang, W. Zhang, R. Cao and H. Zheng, *Adv. Funct. Mater.*, 2024, 2410439.
208 M. F. Lagadec and A. Grimaud, *Nat. Mater.*, 2020, **19**, 1140–1150.
209 M. Elimelech and W. A. Phillip, *Science*, 2011, **333**, 712–717.
210 B. Zhang, C. Zhang, W. Yuan, O. Yang, Y. Liu, L. He, Y. Hu, L. Zhou, J. Wang and Z. L. Wang, *ACS Appl. Mater. Interfaces*, 2022, **14**, 9046–9056.
211 J. Liu, S. Duan, H. Shi, T. Wang, X. Yang, Y. Huang, G. Wu and Q. Li, *Angew. Chem., Int. Ed.*, 2022, **134**, e202210753.
212 F. Dionigi, T. Reier, Z. Pawolek, M. Gliech and P. Strasser, *ChemSusChem*, 2016, **9**, 962–972.
213 R. K. B. Karlsson and A. Cornell, *Chem. Rev.*, 2016, **116**, 2982–3028.
214 Y. Song, G. Jiang, Y. Chen, P. Zhao and Y. Tian, *Sci. Rep.*, 2017, **7**, 6865.
215 E. Baniasadi, I. Dincer and G. F. Naterer, *Int. J. Hydrogen Energy*, 2013, **38**, 2589–2595.
216 Z. Wang, M. Zhang, X. Liu, H. Gao, C. Song and D. Wang, *ACS Appl. Nano Mater.*, 2024, **7**, 6196–6204.
217 A. Malek, Y. Xue and X. Lu, *Angew. Chem., Int. Ed.*, 2023, **62**, e202309854.
218 L. Li, G. Zhang, B. Wang and S. Yang, *Appl. Catal., B*, 2022, **302**, 120847.
219 L. Yu, L. Wu, B. McElhenny, S. Song, D. Luo, F. Zhang, Y. Yu, S. Chen and Z. Ren, *Energy Environ. Sci.*, 2020, **13**, 3439–3446.
220 W. Liu, K. Jiang, Y. Hu, Q. Li, Y. Deng, J. Bao and Y. Lei, *J. Colloid Interface Sci.*, 2021, **604**, 767–775.
221 M. Ning, L. Wu, F. Zhang, D. Wang, S. Song, T. Tong, J. Bao, S. Chen, L. Yu and Z. Ren, *Mater. Today Phys.*, 2021, **19**, 100419.
222 Q. Tu, W. Liu, M. Jiang, W. Wang, Q. Kang, P. Wang, W. Zhou and F. Zhou, *ACS Appl. Energy Mater.*, 2021, **4**, 4630–4637.
223 B. Wang, M. Lu, D. Chen, Q. Zhang, W. Wang, Y. Kang, Z. Fang, G. Pang and S. Feng, *J. Mater. Chem. A*, 2021, **9**, 13562–13569.
224 L. Wu, L. Yu, F. Zhang, B. McElhenny, D. Luo, A. Karim, S. Chen and Z. Ren, *Adv. Funct. Mater.*, 2021, **31**, 2006484.
225 S. Song, Y. Wang, X. Tian, F. Sun, X. Liu, Y. Yuan, W. Li and J. Zang, *J. Colloid Interface Sci.*, 2023, **633**, 668–678.
226 Y. Cheng, Y. Luo, Y. Zheng, J. Pang, K. Sun, J. Hou, G. Wang, W. Guo, X. Guo and L. Chen, *Int. J. Hydrogen Energy*, 2022, **47**, 35655–35665.
227 L. Xiao, J. Han, Z. Wang and J. Guan, *Int. J. Hydrogen Energy*, 2023, **48**, 23776–23784.
228 N. Q. Tran, Q. M. Le, T. T. N. Tran, T.-K. Truong, J. Yu, L. Peng, T. A. Le, T. L. H. Doan and T. B. Phan, *ACS Appl. Mater. Interfaces*, 2024, **16**, 28625–28637.
229 Y. Chen, L. Shen, C. Wang, S. Feng, N. Zhang, K. Zhang and B. Yang, *J. Chem. Eng.*, 2022, **430**, 132632.
230 M. Xiao, C. Wu, J. Zhu, C. Zhang, Y. Li, J. Lyu, W. Zeng, H. Li, L. Chen and S. Mu, *Nano Res.*, 2023, **16**, 8945–8952.
231 J. Liu, J. Yang, Y. Song, J. Sun, Y. Tian, Q. Chen, X. Zhang and L. Zhang, *J. Colloid Interface Sci.*, 2023, **643**, 17–25.
232 N. Xu, F.-L. Wang, J.-Q. Han, W.-L. Yu, W.-J. Li, Y.-C. Li, Y.-L. Zhou, Y.-M. Chai and B. Dong, *Inorg. Chem. Front.*, 2023, **10**, 7193–7203.
233 Z. Qin, W. Liu, W. Que, J. Feng, W. Shi, F. Wu and X. Cao, *ChemPhysMater*, 2023, **2**, 185–196.
234 T. Reier, M. Oezaslan and P. Strasser, *ACS Catal.*, 2012, **2**, 1765–1772.
235 T. Kimura, *Chem. Rec.*, 2016, **16**, 445–457.
236 T. Kimura, *Dalton Trans.*, 2024, **53**, 12434–12441.
237 S. Dutta, K. C. W. Wu and T. Kimura, *Chem. Mater.*, 2015, **27**, 6918–6928.
238 Q. Ma, S. Dutta, K. C. W. Wu and T. Kimura, *Chem. – Eur. J.*, 2018, **24**, 6886–6904.
239 T. Kimura, *J. Nanosci. Nanotechnol.*, 2013, **13**, 2461–2470.
240 T. Kimura, *J. Mater. Chem. A*, 2020, **8**, 25528–25547.
241 S. Piracha, Y. Zhang, A. Raza and G. Li, *Chem. Commun.*, 2024, **60**, 9918–9929.
242 X. Ren, Y. Zhai, N. Yang, B. Wang and S. Liu, *Adv. Funct. Mater.*, 2024, **34**, 2401610.
243 H. Mazhari Abbasi, K. Jafarzadeh and S. M. Mirali, *J. Electroanal. Chem.*, 2016, **777**, 67–74.
244 Y. Xin, Q. Hua, C. Li, H. Zhu, L. Gao, X. Ren, P. Yang and A. Liu, *J. Mater. Chem. A*, 2024, **12**, 23147–23178.

